Commun. Comput. Phys.
doi: 10.4208/cicp.OA-2024-0023

Vol. **36**, No. 1, pp. 1-29
July 2024

High Order Compact Hermite Reconstructions and Their Application in the Improved Two-Stage Fourth Order Time-Stepping Framework for Hyperbolic Problems: Two-Dimensional Case

Ang Li[1], Jiequan Li[2], Juan Cheng[3,*] and Chi-Wang Shu[4]

[1] *Peking University Chongqing Research Institute of Big Data, Chongqing 400000, P.R. China.*
[2] *Academy of Multidisciplinary Studies, Capital Normal University, Beijing 100048, P.R. China.*
[3] *Laboratory of Computational Physics, Institute of Applied Physics and Computational Mathematics, Beijing 100088, P.R. China.*
[4] *Division of Applied Mathematics, Brown University, Providence 02912, RI, USA.*

Received 27 January 2024; Accepted (in revised version) 9 April 2024

Abstract. The accuracy and efficiency of numerical methods are hot topics in computational fluid dynamics. In the previous work [J. Comput. Phys. 355 (2018) 385] of Du et al., a two-stage fourth order (S_2O_4) numerical scheme for hyperbolic conservation laws is proposed, which is based on dimension-by-dimensional HWENO5 and WENO5 reconstructions and GRP solver, and uses a S_2O_4 time-stepping framework. In this paper, we aim to design a new type of S_2O_4 finite volume scheme, to further improve the compactness and efficiency of the numerical scheme. We design an improved S_2O_4 framework for two-dimensional compressible Euler equations, and develop nonlinear compact Hermite reconstructions to avoid oscillations near discontinuities. The new two-stage fourth order numerical schemes based on the above nonlinear compact Hermite reconstructions and GRP solver are high-order, stable, compact, efficient and essentially non-oscillatory. In addition, the above reconstructions and the corresponding numerical schemes are extended to eighth-order accuracy in space, and can be theoretically extended to any even-order accuracy. Finally, we present a large number of numerical examples to verify the excellent performance of the designed numerical schemes.

AMS subject classifications: 65M08, 65M12, 35L65, 76M12

Key words: Hyperbolic conservation laws, two-stage fourth order time-stepping framework, compact Hermite reconstruction, high order, GRP solver.

*Corresponding author. *Email addresses:* liang19@gscaep.ac.cn (A. Li), jiequan@cnu.edu.cn (J. Li), cheng_juan@iapcm.ac.cn (J. Cheng), chi-wang_shu@brown.edu (C.-W. Shu)

1 Introduction

Fluid dynamics plays a crucial role in predicting fluid flow in various fields, such as aerospace engineering, weather forecasting, and more. Among these, the two-dimensional Euler system, which belongs to the class of hyperbolic conservation laws, serves as a classic model. The demand for precise prediction and simulation in these applications has driven the need for high accurate schemes. However, the pursuit of accuracy must be balanced with computational efficiency, making this an interesting and challenging problem. Additionally, in order to capture the details in the flow field more accurately, such as turbulence and shock waves, we need to develop high-resolution schemes, which can be achieved by constructing compact schemes. At the same time, compactness can effectively reduce the communication overhead between nodes, making the scheme more efficient in parallel computing.

For hyperbolic conservation laws, plenty of numerical methods have been developed, including the finite difference method (FDM), finite volume method (FVM), and finite element method (FEM). Specifically, in the realm of FVM, numerous high order schemes such as the essentially non-oscillatory (ENO) [1], weighted ENO (WENO) [2,3], and Hermite WENO (HWENO) [4, 5] schemes have emerged over the past decades. The ENO scheme avoids oscillations by selecting the smoothest stencil. However, this approach disregards valuable data from other stencils. As an advancement, the WENO scheme accepts all stencils in smooth regions to attain higher order accuracy, while concurrently preserving the capacity to avoid oscillations. Subsequently, Qiu and Shu introduced the HWENO scheme. In this scheme, each cell contains an increased degree of freedom, encompassing not only the cell average but also the gradient average. This leads to a more narrow stencil for the HWENO scheme, making it more compact compared to the traditional WENO scheme.

Many of the above schemes adopted the strong-stability preserving Runge-Kutta (SSP-RK) time-stepping methods [6], a multi-stage time-stepping method, such as the third order SSP-RK method, which can achieve third order in time through three time-stages. This method can be expressed as a convex combination of forward Euler method, which implies many nice properties that can be generalized. However, the numerous intermediate time-stages make the resulting scheme less compact. Alternatively, there is a class of time-stepping method known as the Lax-Wendroff type methods [1,7,8], which can achieve high order accuracy in time through one time-stage. The resulting schemes are more compact, but their formulation and coding could be rather complicated, especially for multidimensional systems. Afterwards, a class of multi-stage multi-derivative (MSMD) time-stepping methods [9,10] emerged, which balance the complexity and compactness. Among them, the S_2O_4 framework makes a certain contribution, with many related works [11, 12]. Note that the following S_2O_4 framework here specifically refers to the time-stepping framework proposed in [11], using a Lax-Wendroff type flow solver and a two-moment reconstruction, which is different from the previous one in [9]. Two-

moment reconstruction means that the stencil in each cell contains not only the cell average but also the gradient average.

In the previous work [13], a S_2O_4 scheme is proposed, which is based on dimension-by-dimensional HWENO5 and WENO5 reconstructions and GRP solver, and uses the S_2O_4 time-stepping framework. Particularly, this scheme use the HWENO5 reconstruction to get the function value on the cell interface, and use the HWENO5 and WENO5 reconstruction to get the gradient value, which lacks compactness. If we only choose the HWENO5 reconstruction to get the gradient value, the temporal order of the resulting schemes would reduce from fourth-order to third-order. Besides, the one-dimensional reconstructions are performed dimension-by-dimension in this work. This approach does not ensure symmetry, has high memory requirement, because it needs to scan the meshes twice and store intermediate variables, and is more difficult to be generalized to unstructured meshes.

In this paper, we aim to design a new type of S_2O_4 finite volume scheme, to further improve the compactness and efficiency of the numerical scheme. We specifically design an improved S_2O_4 framework for two-dimensional compressible Euler equations, and develop nonlinear compact Hermite reconstructions. Particularly, by using Taylor analysis, we identify the causes of the order reduction and design the improved S_2O_4 framework, which can accept more types of reconstructions. The improved S_2O_4 framework preserves the temporal order when performing any reconstruction of fourth order or higher. As for the reconstructions, we first develop a genuinely two-dimensional linear compact Hermite reconstruction with second-order and fourth-order accuracy. To avoid oscillations near discontinuities, we combine them with the WENO technique and hybrid choice strategy, respectively, and obtain two nonlinear compact Hermite reconstructions. These reconstructions are more compact than the HWENO5 reconstruction, and also more compact than the WENO5 reconstruction. Note that these two-dimensional Hermite reconstructions can be regarded as the generalization of our one-dimensional Hermite reconstructions [14]. Based on the above nonlinear compact Hermite reconstructions and GRP solver, we obtain the corresponding S_2O_4 schemes, which have fourth order accuracy both in space and time, and are stable, compact, efficient and essentially non-oscillatory. As a continuation of this work, the above reconstructions and the corresponding numerical schemes are extended to eighth-order accuracy in space. Theoretically, this approach has the potential to be generalized to any $2k$-th order accuracy. Finally, a large number of numerical examples validate the excellent performance of the designed numerical schemes.

This paper is organized as follows. In Section 2, we propose an improved S_2O_4 framework. In Section 3, we provide a detailed description of our linear Hermite reconstructions, using $k=1,2,4$ as examples. In Section 4, we develop two versions of nonlinear reconstructions for $k=2,4$. In Section 5, we provide several numerical examples to demonstrate the performance of our schemes. Finally, in Section 6, we give the concluding remarks.

2 An improved S_2O_4 framework

Generally, two-dimensional hyperbolic conservation laws can be expressed as:

$$\partial_t \boldsymbol{u}+\partial_x \boldsymbol{f}(\boldsymbol{u})+\partial_y \boldsymbol{g}(\boldsymbol{u})=0, \quad x,y\in\mathbb{R}, \quad t>0, \tag{2.1}$$

where $\boldsymbol{u}$ is the vector of the conservative variables and $\boldsymbol{f}(\boldsymbol{u})$, $\boldsymbol{g}(\boldsymbol{u})$ are the corresponding flux vectors. The computation cell is $I_{ij}=[x_{i-\frac{1}{2}},x_{i+\frac{1}{2}}]\times[y_{j-\frac{1}{2}},y_{j+\frac{1}{2}}]$ with the cell size $h_x=x_{i+\frac{1}{2}}-x_{i-\frac{1}{2}}$, $i=1,\cdots,N_x$ and $h_y=y_{j+\frac{1}{2}}-y_{j-\frac{1}{2}}$, $j=1,\cdots,N_y$, and the uniform meshes are taken for simplicity. Note that the framework is also applicable for nonuniform meshes. The cell averages of $\boldsymbol{u}(x,y)$ and its gradient $\nabla\boldsymbol{u}$, denoted as $\bar{\boldsymbol{u}}_{ij}$ and $(\bar{\boldsymbol{v}}_{ij},\bar{\boldsymbol{w}}_{ij})$ respectively, which are defined for each cell and can be expressed as

$$\bar{\boldsymbol{u}}_{ij}=\frac{1}{h_xh_y}\iint_{I_{ij}}\boldsymbol{u}(x,y)dxdy, \quad (\bar{\boldsymbol{v}}_{ij},\bar{\boldsymbol{w}}_{ij})=\frac{1}{h_xh_y}\iint_{I_{ij}}\nabla\boldsymbol{u}(x,y)dxdy. \tag{2.2}$$

Subsequently, we present our improved S_2O_4 framework, based on the original framework proposed in [11], and introduce its computational process as follows. The time levels are assumed to be t^n, $n=0,1,\cdots$, the time step is defined as $\tau^n=t^{n+1}-t^n$, and the superscript n will be omitted if no ambiguity is caused.

Step 1. At the time level $t=t^n$, given the cell average $\bar{\boldsymbol{u}}_{ij}^n$ and the gradient average $(\bar{\boldsymbol{v}}_{ij}^n,\bar{\boldsymbol{w}}_{ij}^n)$, the generalized Riemann solution at the two Gaussian points on each cell interface can be obtained by using appropriate reconstruction and Lax-Wendroff type flow solver. Specifically, by using appropriate reconstruction, which refers to the process of reconstructing the solution at the cell interfaces from the cell averages and the gradient averages, represented by the operator $\mathcal{R}$, we obtain the values at one of the Gaussian points at the cell interfaces:

$$\begin{aligned}&\left(\boldsymbol{u}^n_{(i+\frac{1}{2},-),j+G},(\partial_x\boldsymbol{u})^n_{(i+\frac{1}{2},-),j+G},(\partial_y\boldsymbol{u})^n_{(i+\frac{1}{2},-),j+G},\right.\\&\left.(\partial_x^2\boldsymbol{u})^n_{(i+\frac{1}{2},-),j+G},(\partial_x\partial_y\boldsymbol{u})^n_{(i+\frac{1}{2},-),j+G},\left(\partial_y^2\boldsymbol{u}\right)^n_{(i+\frac{1}{2},-),j+G}\right)=\mathcal{R}(\bar{\boldsymbol{u}}^n_{ij},\bar{\boldsymbol{v}}^n_{ij},\bar{\boldsymbol{w}}^n_{ij},\cdots),\end{aligned} \tag{2.3}$$

where $G=\sqrt{3}/6$. Then we have an associated generalized Riemann problem (GRP) with the initial condition at the time level $t=t^n$,

$$\begin{aligned}&\boldsymbol{u}(x,y,t^n)=\begin{cases}\boldsymbol{p}_L(x,y), & x<x_{i+\frac{1}{2}},\\ \boldsymbol{p}_R(x,y), & x>x_{i+\frac{1}{2}},\end{cases}\\&\boldsymbol{p}_L(x,y)=\boldsymbol{u}^n_{(i+\frac{1}{2},-),j+G}+(\partial_x\boldsymbol{u})^n_{(i+\frac{1}{2},-),j+G}(x-x_{i+\frac{1}{2}})+(\partial_y\boldsymbol{u})^n_{(i+\frac{1}{2},-),j+G}(y-y_{j+G}),\\&\boldsymbol{p}_R(x,y)=\boldsymbol{u}^n_{(i+\frac{1}{2},+),j+G}+(\partial_x\boldsymbol{u})^n_{(i+\frac{1}{2},+),j+G}(x-x_{i+\frac{1}{2}})+(\partial_y\boldsymbol{u})^n_{(i+\frac{1}{2},+),j+G}(y-y_{j+G}).\end{aligned} \tag{2.4}$$

Subsequently, the generalized Riemann solution $\left(\boldsymbol{u}^{n,+}_{i+\frac{1}{2},j+G},(\partial_t\boldsymbol{u})^{n,+}_{i+\frac{1}{2},j+G}\right)$ is obtained by the Lax-Wendroff type flow solver, such as the GRP solver [15], which is the exact (or

approximate) limit of the solution of the associated GRP,

$$\boldsymbol{u}^{n,+}_{i+\frac{1}{2},j+G}=\lim_{t\to t^n,+}\boldsymbol{u}(x_{i+\frac{1}{2}},y_{j+G},t),\quad (\partial_t\boldsymbol{u})^{n,+}_{i+\frac{1}{2},j+G}=\lim_{t\to t^n,+}\partial_t\boldsymbol{u}(x_{i+\frac{1}{2}},y_{j+G},t). \tag{2.5}$$

This Lax-Wendroff type flow solver is represented by the operator $\mathcal{G}$, and we have

$$\left(\boldsymbol{u}^{n,+}_{i+\frac{1}{2},j+G},(\partial_t\boldsymbol{u})^{n,+}_{i+\frac{1}{2},j+G}\right)=\mathcal{G}\left(\boldsymbol{u}^{n}_{(i+\frac{1}{2},\pm),j+G},(\partial_x\boldsymbol{u})^{n}_{(i+\frac{1}{2},\pm),j+G},(\partial_y\boldsymbol{u})^{n}_{(i+\frac{1}{2},\pm),j+G}\right). \tag{2.6}$$

The second derivative $\left(\partial_t^2\boldsymbol{u}\right)^{n,+}_{i+\frac{1}{2},j+G}$ is obtained by taking the derivatives of the PDE. For more details, please refer to Appendix A.

The same procedure is for all other Gaussian points.

Step 2. For the first time-stage, the cell average $\bar{\boldsymbol{u}}^{n+\frac{1}{2}}_{ij}$ and the gradient average $(\bar{\boldsymbol{v}}^{n+\frac{1}{2}}_{ij},\bar{\boldsymbol{w}}^{n+\frac{1}{2}}_{ij})$ at the time level $t=t^{n+\frac{1}{2}}$ are obtained using the following formulae

$$\begin{aligned}
&\bar{\boldsymbol{u}}^{n+\frac{1}{2}}_{ij}=\bar{\boldsymbol{u}}^{n}_{i,j}-\frac{\tau}{2h_x}\left(\hat{\boldsymbol{f}}^{*}_{i+\frac{1}{2},j}-\hat{\boldsymbol{f}}^{*}_{i-\frac{1}{2},j}\right)-\frac{\tau}{2h_y}\left(\hat{\boldsymbol{g}}^{*}_{i,j+\frac{1}{2}}-\hat{\boldsymbol{g}}^{*}_{i,j-\frac{1}{2}}\right),\\
&\bar{\boldsymbol{v}}^{n+\frac{1}{2}}_{ij}=\frac{1}{h_x}\left(\hat{\boldsymbol{u}}^{n+\frac{1}{2}}_{i+\frac{1}{2},j}-\hat{\boldsymbol{u}}^{n+\frac{1}{2}}_{i-\frac{1}{2},j}\right),\quad \bar{\boldsymbol{w}}^{n+\frac{1}{2}}_{ij}=\frac{1}{h_y}\left(\hat{\boldsymbol{u}}^{n+\frac{1}{2}}_{i,j+\frac{1}{2}}-\hat{\boldsymbol{u}}^{n+\frac{1}{2}}_{i,j-\frac{1}{2}}\right),
\end{aligned} \tag{2.7}$$

where the numerical flux $\hat{\boldsymbol{f}}^{*}_{i+\frac{1}{2},j}$ and the line average along the interface $\hat{\boldsymbol{u}}^{n+\frac{1}{2}}_{i+\frac{1}{2},j}$ are obtained by Gaussian integral:

$$\hat{\boldsymbol{f}}^{*}_{i+\frac{1}{2},j}=\frac{1}{2}\left(\hat{\boldsymbol{f}}^{*}_{i+\frac{1}{2},j+G}+\hat{\boldsymbol{f}}^{*}_{i+\frac{1}{2},j-G}\right),\quad \hat{\boldsymbol{u}}^{n+\frac{1}{2}}_{i+\frac{1}{2},j}=\frac{1}{2}\left(\hat{\boldsymbol{u}}^{n+\frac{1}{2}}_{i+\frac{1}{2},j+G}+\hat{\boldsymbol{u}}^{n+\frac{1}{2}}_{i+\frac{1}{2},j-G}\right), \tag{2.8}$$

and the numerical flux and the interface value at the Gaussian points $(x_{i+\frac{1}{2}},y_{j\pm G})$ are defined as

$$\begin{aligned}
&\hat{\boldsymbol{f}}^{*}_{i+\frac{1}{2},j\pm G}=\boldsymbol{f}\left(\boldsymbol{u}^{n,+}_{i+\frac{1}{2},j\pm G}\right)+\frac{\tau}{4}\left(\partial_t\boldsymbol{f}\right)^{n,+}_{i+\frac{1}{2},j\pm G},\\
&\hat{\boldsymbol{u}}^{n+\frac{1}{2}}_{i+\frac{1}{2},j\pm G}=\boldsymbol{u}^{n,+}_{i+\frac{1}{2},j\pm G}+\frac{\tau}{2}\left(\partial_t\boldsymbol{u}\right)^{n,+}_{i+\frac{1}{2},j\pm G}+\frac{\tau^2}{8}\left(\partial_t^2\boldsymbol{u}\right)^{n,+}_{i+\frac{1}{2},j\pm G},
\end{aligned} \tag{2.9}$$

where $\left(\partial_t\boldsymbol{f}\right)^{n,+}_{i+\frac{1}{2},j\pm G}=\frac{\partial\boldsymbol{f}}{\partial\boldsymbol{u}}\left(\boldsymbol{u}^{n,+}_{i+\frac{1}{2},j\pm G}\right)\left(\partial_t\boldsymbol{u}\right)^{n,+}_{i+\frac{1}{2},j\pm G}$.

In the y direction, $\hat{\boldsymbol{g}}^{*}_{i,j+\frac{1}{2}}$ and $\hat{\boldsymbol{u}}^{n+\frac{1}{2}}_{i,j+\frac{1}{2}}$ are defined similarly.

Step 3. At the middle time level $t=t^{n+\frac{1}{2}}$, the generalized Riemann solution at each Gaussian point, such as $\left(\boldsymbol{u}^{n+\frac{1}{2},+}_{i+\frac{1}{2},j+G},(\partial_t\boldsymbol{u})^{n+\frac{1}{2},+}_{i+\frac{1}{2},j+G}\right)$, can be obtained in a similar way as the first step. Note that there is no need to calculate the second spatial derivatives $\left(\partial_x^2\boldsymbol{u}\right)^{n+\frac{1}{2}}_{(i+\frac{1}{2},-),j+G}$, $\left(\partial_x\partial_y\boldsymbol{u}\right)^{n+\frac{1}{2}}_{(i+\frac{1}{2},-),j+G}$ and $\left(\partial_y^2\boldsymbol{u}\right)^{n+\frac{1}{2}}_{(i+\frac{1}{2},-),j+G}$, and the second temporal derivative $\left(\partial_t^2\boldsymbol{u}\right)^{n+\frac{1}{2},+}_{i+\frac{1}{2},j+G}$ at each Gaussian point.

Step 4. For the second time-stage, the cell average $\bar{\boldsymbol{u}}_{ij}^{n+1}$ and the gradient average $(\bar{\boldsymbol{v}}_{ij}^{n+1},\bar{\boldsymbol{w}}_{ij}^{n+1})$ at the next time level $t=t^{n+1}$ is derived from the following formulae

$$\begin{aligned}
&\bar{\boldsymbol{u}}_{ij}^{n+1}=\bar{\boldsymbol{u}}_{i,j}^{n}-\frac{\tau}{h_x}\left(\hat{\boldsymbol{f}}_{i+\frac{1}{2},j}^{4th}-\hat{\boldsymbol{f}}_{i-\frac{1}{2},j}^{4th}\right)-\frac{\tau}{h_y}\left(\hat{\boldsymbol{g}}_{i,j+\frac{1}{2}}^{4th}-\hat{\boldsymbol{g}}_{i,j-\frac{1}{2}}^{4th}\right),\\
&\bar{\boldsymbol{v}}_{ij}^{n+1}=\frac{1}{h_x}\left(\hat{\boldsymbol{u}}_{i+\frac{1}{2},j}^{n+1}-\hat{\boldsymbol{u}}_{i-\frac{1}{2},j}^{n+1}\right),\quad \bar{\boldsymbol{w}}_{ij}^{n+1}=\frac{1}{h_y}\left(\hat{\boldsymbol{u}}_{i,j+\frac{1}{2}}^{n+1}-\hat{\boldsymbol{u}}_{i,j-\frac{1}{2}}^{n+1}\right),
\end{aligned}\tag{2.10}$$

where the numerical flux $\hat{\boldsymbol{f}}_{i+\frac{1}{2},j}^{4th}$ and the line average along the interface $\hat{\boldsymbol{u}}_{i+\frac{1}{2},j}^{n+1}$ are also derived by similar Gaussian integral as (2.8), and the numerical flux and the interface value at the Gaussian points $(x_{i+\frac{1}{2}},y_{j\pm G})$ are defined as

$$\begin{aligned}
&\hat{\boldsymbol{f}}_{i+\frac{1}{2},j\pm G}^{4th}=\boldsymbol{f}\left(\boldsymbol{u}_{i+\frac{1}{2},j\pm G}^{n,+}\right)+\frac{\tau}{6}\left(\partial_t\boldsymbol{f}\right)_{i+\frac{1}{2},j\pm G}^{n,+}+\frac{\tau}{3}\left(\partial_t\boldsymbol{f}\right)_{i+\frac{1}{2},j\pm G}^{n+\frac{1}{2},+},\\
&\hat{\boldsymbol{u}}_{i+\frac{1}{2},j\pm G}^{n+1}=\boldsymbol{u}_{i+\frac{1}{2},j\pm G}^{n,+}+\tau\left(\partial_t\boldsymbol{u}\right)_{i+\frac{1}{2},j\pm G}^{n+\frac{1}{2},+},
\end{aligned}\tag{2.11}$$

where $\left(\partial_t\boldsymbol{f}\right)_{i+\frac{1}{2},j\pm G}^{n+\frac{1}{2},+}=\frac{\partial \boldsymbol{f}}{\partial \boldsymbol{u}}\left(\boldsymbol{u}_{i+\frac{1}{2},j\pm G}^{n+\frac{1}{2},+}\right)\left(\partial_t\boldsymbol{u}\right)_{i+\frac{1}{2},j\pm G}^{n+\frac{1}{2},+}$.

In the y direction, $\hat{\boldsymbol{g}}_{i,j+\frac{1}{2}}^{4th}$ and $\hat{\boldsymbol{u}}_{i,j+\frac{1}{2}}^{n+1}$ are defined similarly.

Under the original framework, numerical experiments show that using gradient averages as input for the reconstruction of gradients, reduces the temporal order from fourth-order to third-order. Thus, we introduce the second derivative $\left(\partial_t^2\boldsymbol{u}\right)_{i+\frac{1}{2},j\pm G}^{n,+}$ in (2.9) to improve the original S_2O_4 framework, which allows our framework to adopt more types of reconstructions while keeping the fourth temporal order. We provide a detailed Taylor analysis of the improved S_2O_4 framework applied to linear equations in Appendix B, in order to check the order of accuracy. We also briefly analyze how the temporal order of the original framework degenerates under specific reconstructions.

3 Linear Hermite reconstructions

In this section, we turn our attention to the linear Hermite reconstruction in two-dimensional case. We hope the reconstruction is more compact than the previous dimension-by-dimensional HWENO5 reconstruction in [13]. And it is fourth order, which is more suitable for the S_2O_4 framework. Building upon the foundation of Hermite reconstructions of $2k$-th order accuracy in one-dimensional case, as presented in [14], we generalize them to two-dimensional case, while preserving similar performance.

In the case of $2k$-th order reconstruction, we have k^2 potential candidate stencils

$$S_{rs}(i,j)=\bigcup_{m=0}^{k-1}\bigcup_{\ell=0}^{k-1}I_{i-r+m,j-s+\ell},\quad r,s=0,1,\cdots,k-1,\quad k\geqslant 1.\tag{3.1}$$

And the Hermite reconstructions $p_{ij}^{rs}(x,y)$ are defined over these stencils for the given cell averages of a function $u(x,y)$ and its gradient $\nabla u=(v,w)$,

$$\overline{u}_{ij}=\frac{1}{h_x h_y}\int_{I_{ij}} u(x,y)dxdy, \quad (\overline{v}_{ij},\overline{w}_{ij})=\frac{1}{h_x h_y}\int_{I_{ij}} \nabla u(x,y)dxdy, \tag{3.2}$$

where the definition of symbols related to the meshes remains consistent with that established in Section 2. The superscripts r and s in $p_{ij}^{rs}(x,y)$, indicate that these values depend on the stencil $S_{rs}(i,j)$ and will be omitted if no ambiguity is caused.

Such a reconstruction should approximate $u(x,y)$ within $2k$-th order accuracy inside each cell I_{ij},

$$p_{ij}(x,y)=u(x,y)+\mathcal{O}(h^{2k}), \tag{3.3}$$

and its derivatives of each order satisfy

$$\partial_x^{d_1}\partial_y^{d_2}p_{ij}(x,y)=\partial_x^{d_1}\partial_y^{d_2}u(x,y)+\mathcal{O}(h^{2k-d_1-d_2}), \quad d_1+d_2\leqslant 2k-1. \tag{3.4}$$

In particular, it is $2k$-th order accurate at Gaussian points at the cell interfaces.

Furthermore, we aim to construct a two-dimensional reconstruction that can degrade to the one-dimensional reconstruction we previously gave in [14]. This paves the way for us to anticipate that the two-dimensional reconstruction will achieve similar good performance. We also observe that the stencil S_{rs} contains a total of k^2 cells and $3k^2$ degrees of freedom. In the $\mathcal{P}^{2k-1}$ space, constructing a $2k$-th order reconstruction only requires $2k^2+k$ degrees of freedom. When $k=1$, this is precisely equivalent, but when $k>1$, there are redundant degrees of freedom, which may require least squares or other techniques. However, in this paper, we believe that the computational cost of least squares is quite high, so we seek another solution. We eliminate k^2-k degrees of freedom, so that the degrees of freedom can just construct a $2k$-th order reconstruction. Moreover, we need to make the final stencil as symmetrical as possible and ensure that the target cell I_{ij} itself is always in the stencil.

Finally, we synthesize the requirements mentioned above and obtain the stencils by the following steps.

1. In the case of $k=1$, the single stencil selection is depicted in Fig. 1(a). In this figure, the cell average $\bar{u}_{ij}$ is symbolized by a circle, while the gradient average $\bar{v}_{ij}$ or $\bar{w}_{ij}$ is represented by an arrow. The domain, where the polynomial reconstructed by this stencil is applied, is delineated by the blue line. The polynomial is expressed as

$$p_{ij}(x,y)=\bar{u}_{ij}+\bar{v}_{ij}(x-x_i)+\bar{w}_{ij}(y-y_j). \tag{3.5}$$

2. In the case of $k=2$, we obtain two viable stencils, as depicted in Fig. 1(b) and Fig. 1(c). Upon conducting a series of straightforward tests, we discover that both stencils demonstrate comparable performance. For the computations in this paper,

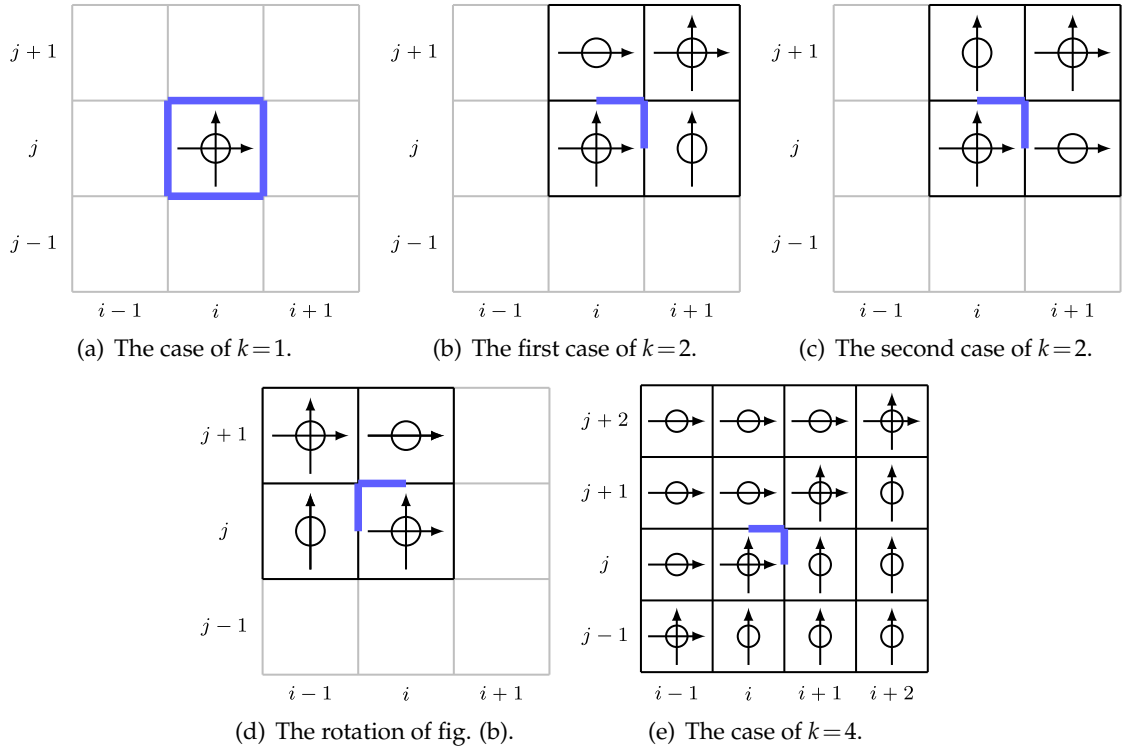

(a) The case of $k=1$. (b) The first case of $k=2$. (c) The second case of $k=2$.

(d) The rotation of fig. (b). (e) The case of $k=4$.

Figure 1: Graphical representation of the stencil for $k=1,2,4$. The cell average $\bar{u}_{ij}$ is symbolized by a circle, the gradient average $\bar{v}_{ij}$ is represented by an right arrow, and the gradient average $\bar{w}_{ij}$ is represented by an upper arrow. The domain, where the polynomial reconstructed by this stencil is applied, is delineated by the blue line.

we opt for the first stencil depicted in Fig. 1(b). It is crucial to note that this stencil is applicable solely to a quarter of the cell interfaces. The values at the remaining cell interfaces are provided by the rotated stencil, as depicted in Fig. 1(d). Hence there are four stencils for the reconstructions in one cell. The expression of the polynomial is relatively complex and will not be displayed. The polynomial values at the Gaussian point $(x_{i+\frac{1}{2}},y_{j+G})$ on the uniform meshes can be represented as

$$\begin{aligned}&\left(\partial_x^{d_1}\partial_y^{d_2}u\right)_{(i+\frac{1}{2},-),j+G}=\partial_x^{d_1}\partial_y^{d_2}p_{ij}(x_{i+\frac{1}{2}},y_{j+G})\\&=\frac{1}{h_x^{d_1}h_y^{d_2}}\sum_{m=0}^{1}\sum_{\ell=0}^{1}\left(\phi_{m,\ell}^{d_1,d_2}\bar{u}_{i+m,j+\ell}+h_x\psi_{m,\ell}^{d_1,d_2}\bar{v}_{i+m,j+\ell}+h_y\sigma_{m,\ell}^{d_1,d_2}\bar{w}_{i+m,j+\ell}\right).\end{aligned}\tag{3.6}$$

When the orders of the derivatives d_1 and d_2 are equal to zero, the expression corresponds to the polynomial itself. The coefficients $\phi_{m,\ell}^{d_1,d_2}$, $\psi_{m,\ell}^{d_1,d_2}$ and $\sigma_{m,\ell}^{d_1,d_2}$ are detailed in Table 1. Note that the polynomial values at the other Gaussian points can be obtained by simple transformation of (3.6).

Table 1: The coefficients in (3.6).

(d_1,d_2)	$\phi_{0,0}^{d_1,d_2}$ $\psi_{0,0}^{d_1,d_2}$	$\phi_{0,1}^{d_1,d_2}$ $\psi_{0,1}^{d_1,d_2}$	$\phi_{1,0}^{d_1,d_2}$ $\psi_{1,1}^{d_1,d_2}$	$\phi_{1,1}^{d_1,d_2}$ $\sigma_{0,0}^{d_1,d_2}$	$\sigma_{1,0}^{d_1,d_2}$	$\sigma_{1,1}^{d_1,d_2}$
(0, 0)	$(15-\sqrt{3})/18$ $(6-\sqrt{3})/18$	$(\sqrt{3}-6)/18$ $(\sqrt{3}-3)/18$	$1/6$ $-1/6$	$1/3$ $\sqrt{3}/12$	$\sqrt{3}/18$	$-\sqrt{3}/36$
(1, 0)	-1 0	-1 $-1/2$	1 $-1/2$	1 $-\sqrt{3}/6$	$\sqrt{3}/6$	0
(0, 1)	$-(2+\sqrt{3})/6$ $-1/3$	$(2+\sqrt{3})/6$ $1/3$	$(2-5\sqrt{3})/6$ 0	$-(2-5\sqrt{3})/6$ $(3-\sqrt{3})/6$	$(3-\sqrt{3})/6$	$-\sqrt{3}/3$
(2, 0)	$(\sqrt{3}-6)/3$ $(\sqrt{3}-6)/3$	$(6-\sqrt{3})/3$ $(3-\sqrt{3})/3$	$(6-\sqrt{3})/3$ 1	$(\sqrt{3}-6)/3$ 0	0	0
(1, 1)	$\sqrt{3}/3$ 0	$-\sqrt{3}/3$ 0	$\sqrt{3}/3$ 0	$\sqrt{3}/3$ $(\sqrt{3}-3)/3$	$(3-\sqrt{3})/3$	0
(0, 2)	-1 0	1 0	$2\sqrt{3}-5$ 0	$5-2\sqrt{3}$ -1	$\sqrt{3}-3$	$\sqrt{3}-2$

3. In the case of $k=3$, we observe that our one-dimensional scheme exhibits linear stability. However, upon application to numerical examples, we encounter instability issues when tasked with solving nonlinear equations, such as Euler equations. Hence we do not generalize this reconstruction to the two-dimensional case.

4. In the case of $k=4$, we have about 5.982×10^{11} potential choices that satisfy the above requirements, making it unfeasible to enumerate all potential stencils. Nevertheless, drawing upon our experience with $k=2$, we propose a viable stencil, as depicted in Fig. 1(e). The other three stencils are also provided by rotation operations.

So far, we have obtained two-dimensional reconstructions of second, fourth, and eighth order accuracy, which are extensions of their corresponding one-dimensional reconstructions. These reconstructions are denoted as HC-2, HC-4, and HC-8, respectively, where "HC" stands for "Hermite Construction".

4 Nonlinear Hermite reconstructions

In our pursuit to maintain high order accuracy in smooth regions and effectively prevent oscillations in the vicinity of discontinuities, we have developed two versions of essentially non-oscillatory nonlinear reconstructions.

4.1 Weighted Hermite reconstructions

The nonlinear WENO reconstruction, as proposed in [16], represents a novel approach in this field. This has led to plenty of subsequent studies aimed at refining stencil selection, including the development of the CWENO [17,18] and WENO-AO [19] schemes. These advanced techniques are capable of combining several constructions of different orders.

In Section 3, we obtain the linear reconstructions of second, fourth, and eighth order accuracy. It is worth noting that the reconstruction of second order accuracy coincides with the reconstruction used in the GRP scheme [15], which has demonstrated excellent performance in handling oscillations. In order to achieve comparable performance, we also apply the same minmod limiter to (3.5), resulting in

$$\begin{aligned}
&\bar{v}_{ij}^{lim}=\frac{1}{h_x}\text{minmod}(\alpha(\bar{u}_{i+1,j}-\bar{u}_{ij}),h_x\bar{v}_{ij},\alpha(\bar{u}_{ij}-\bar{u}_{i-1,j})),\\
&\bar{w}_{ij}^{lim}=\frac{1}{h_y}\text{minmod}(\alpha(\bar{u}_{i,j+1}-\bar{u}_{ij}),h_y\bar{w}_{ij},\alpha(\bar{u}_{ij}-\bar{u}_{i,j-1})),\\
&p_{ij}^{s}(x,y)=\bar{u}_{ij}+\bar{v}_{ij}^{lim}(x-x_i)+\bar{w}_{ij}^{lim}(y-y_j),
\end{aligned}\tag{4.1}$$

where the parameter α lies within the interval $[1,2)$. In the numerical examples in this paper, we set the value of α to 1.9. The symbol "s" is utilized to denote that this expression is derived from the second order reconstruction. In this section, our focus is solely on the value of the polynomial at Gaussian points:

$$u^{s}_{(i+\frac{1}{2},-),j+G}=p_{ij}^{s}(x_{i+\frac{1}{2}},y_{j+G}),\quad \left(\partial_x^{d_1}\partial_y^{d_2}u\right)^{s}_{(i+\frac{1}{2},-),j+G}=\partial_x^{d_1}\partial_y^{d_2}p_{ij}^{s}(x_{i+\frac{1}{2}},y_{j+G}).\tag{4.2}$$

On the other hand, the fourth order reconstruction is precisely suitable for the S_2O_4 framework, thereby we can anticipate a fourth order accuracy in smooth regions. Similarly, we define the notation

$$u^{f}_{(i+\frac{1}{2},-),j+G}=p_{ij}^{f}(x_{i+\frac{1}{2}},y_{j+G}),\quad \left(\partial_x^{d_1}\partial_y^{d_2}u\right)^{f}_{(i+\frac{1}{2},-),j+G}=\partial_x^{d_1}\partial_y^{d_2}p_{ij}^{f}(x_{i+\frac{1}{2}},y_{j+G}),\tag{4.3}$$

which are derived from the fourth order reconstruction, where "f" denotes fourth order.

Now, we draw upon the techniques of CWENO and WENO-AO schemes to derive our weighted reconstruction. The value $u^{f}_{(i+\frac{1}{2},-),j+G}$, obtained from the fourth order reconstruction, is rewritten as

$$u^{f}_{(i+\frac{1}{2},-),j+G}=\gamma_s u^{s}_{(i+\frac{1}{2},-),j+G}+\gamma_f\left(\frac{1}{\gamma_f}u^{f}_{(i+\frac{1}{2},-),j+G}-\frac{\gamma_s}{\gamma_f}u^{s}_{(i+\frac{1}{2},-),j+G}\right),\quad \gamma_s+\gamma_f=1.\tag{4.4}$$

Subsequently, the linear weights γ_o are substituted with nonlinear weights ω_o, where $o=s,f$, resulting in

$$u^{\text{WHC-4}}_{(i+\frac{1}{2},-),j+G}=\omega_s u^{s}_{(i+\frac{1}{2},-),j+G}+\omega_f\left(\frac{1}{\gamma_f}u^{f}_{(i+\frac{1}{2},-),j+G}-\frac{\gamma_s}{\gamma_f}u^{s}_{(i+\frac{1}{2},-),j+G}\right),\quad \omega_s+\omega_f=1.\tag{4.5}$$

Here, the superscript "WHC" stands for "Weighted Hermite Construction", and the corresponding reconstruction is referred to as the WHC-4 reconstruction. This expression can be further simplified to

$$u^{\text{WHC-4}}_{(i+\frac{1}{2},-),j+G}=\frac{\omega_f}{\gamma_f}u^f_{(i+\frac{1}{2},-),j+G}+\left(1-\frac{\omega_f}{\gamma_f}\right)u^s_{(i+\frac{1}{2},-),j+G}. \tag{4.6}$$

The nonlinear weights in this study are defined the same way as that in [14], with inspiration drawn from the WENO-Z scheme as detailed in [20]. These weights are expressed as

$$\omega_o=\frac{\alpha_o}{\alpha_s+\alpha_f},\quad \alpha_o=\gamma_o\left(1+\left(\frac{\theta}{\beta_o+\varepsilon}\right)^q\right),\quad o=s,f. \tag{4.7}$$

The variable θ is defined as the absolute difference between β_s and β_f, i.e., $\theta=|\beta_s-\beta_f|$. The diminutive value ε can be expressed as $\widehat{C}h^3$, where $\widehat{C}$ is set to 100 in our numerical examples. The power q is set to 2.

The smoothness indicators β_s and β_f are similar as those used in [16], which are defined as

$$\beta_o=\sum_{d_1+d_2\geqslant 1}\iint_{I_{ij}}h_x^{2d_1-1}h_y^{2d_2-1}\left(\partial_x^{d_1}\partial_y^{d_2}p^o_{ij}(x,y)\right)^2dxdy,\quad o=s,f. \tag{4.8}$$

Specifically, on the uniform meshes, the expressions can be written as

$$\beta_s=(h_x\bar{v}_{ij})^2+(h_y\bar{w}_{ij})^2, \tag{4.9}$$

and

$$\begin{aligned}
&\beta_f=\boldsymbol{U}^\top\boldsymbol{A}\boldsymbol{U},\\
&\boldsymbol{U}=\left[\bar{u}_{ij},\bar{u}_{i,j+1},\bar{u}_{i+1,j},\bar{u}_{i+1,j+1},h_x\bar{v}_{ij},h_x\bar{v}_{i,j+1},h_x\bar{v}_{i+1,j+1},h_y\bar{w}_{ij},h_y\bar{w}_{i+1,j},h_y\bar{w}_{i+1,j+1}\right]^\top,\\
&\boldsymbol{A}=\begin{bmatrix}
\frac{577}{30} & -\frac{187}{15} & -\frac{187}{15} & -\frac{203}{15} & \frac{102}{5} & -\frac{46}{15} & \frac{26}{3} & \frac{102}{5} & -\frac{46}{15} & \frac{26}{3}\\
0 & \frac{5653}{30} & -\frac{203}{15} & -\frac{5263}{15} & \frac{28}{5} & \frac{2779}{15} & \frac{2603}{15} & -\frac{102}{5} & \frac{46}{15} & -\frac{26}{3}\\
0 & 0 & \frac{5653}{30} & -\frac{5263}{15} & -\frac{102}{5} & \frac{46}{15} & -\frac{26}{3} & \frac{28}{5} & \frac{2779}{15} & \frac{2603}{15}\\
0 & 0 & 0 & \frac{10729}{30} & -\frac{28}{5} & -\frac{2779}{15} & -\frac{2603}{15} & -\frac{28}{5} & -\frac{2779}{15} & -\frac{2603}{15}\\
0 & 0 & 0 & 0 & \frac{56}{5} & -\frac{46}{15} & \frac{26}{3} & \frac{7}{3} & -\frac{7}{3} & 0\\
0 & 0 & 0 & 0 & 0 & \frac{197}{4} & \frac{2603}{30} & -\frac{7}{3} & \frac{7}{3} & 0\\
0 & 0 & 0 & 0 & 0 & 0 & \frac{2603}{60} & 0 & 0 & 0\\
0 & 0 & 0 & 0 & 0 & 0 & 0 & \frac{56}{5} & -\frac{46}{15} & \frac{26}{3}\\
0 & 0 & 0 & 0 & 0 & 0 & 0 & 0 & \frac{197}{4} & \frac{2603}{30}\\
0 & 0 & 0 & 0 & 0 & 0 & 0 & 0 & 0 & \frac{2603}{60}
\end{bmatrix}.
\end{aligned} \tag{4.10}$$

With the same nonlinear weights, as defined in (4.7), we can obtain the first and second derivatives at Gaussian points:

$$\left(\partial_x^{d_1}\partial_y^{d_2}u\right)^{\text{WHC-4}}_{(i+\frac{1}{2},-),j+G}=\frac{\omega_f}{\gamma_f}\left(\partial_x^{d_1}\partial_y^{d_2}u\right)^f_{(i+\frac{1}{2},-),j+G}+\left(1-\frac{\omega_f}{\gamma_f}\right)\left(\partial_x^{d_1}\partial_y^{d_2}u\right)^s_{(i+\frac{1}{2},-),j+G}. \tag{4.11}$$

No extra effort is expended in the determination of these nonlinear weights. In a practical setting, the values of the linear weights γ_s and γ_f are typically chosen to be 0.1 and 0.9, respectively.

We have now obtained the fourth order Hermite weighted reconstruction. Next, we will proceed to verify the properties of this reconstruction. Without loss of generality, we assume that the meshes are uniform square, i.e., $h_x=h_y=h$. This leads to a Taylor expansion for the smoothness indicators in smooth regions, similar to the one-dimensional case:

$$\begin{aligned}&\beta_s=\xi_1h^2+\frac{1}{12}\xi_3h^4+\mathcal{O}(h^6),\quad \beta_f=\xi_1h^2+\frac{1}{12}(\xi_2+\xi_3)h^4+\mathcal{O}(h^6),\\&\theta=|\beta_s-\beta_f|=\frac{1}{12}\xi_2h^4+\mathcal{O}(h^6),\end{aligned}\tag{4.12}$$

where ξ_1, ξ_2 and ξ_3 are calculated from the derivative defined at (x_i,y_j),

$$\begin{aligned}&\xi_1=(\partial_xu)^2+(\partial_yu)^2,\quad \xi_2=13\left(\partial_x^2u\right)^2+14\left(\partial_x\partial_yu\right)^2+13\left(\partial_y^2u\right)^2,\\&\xi_3=\partial_xu\left(\partial_x^3u+\partial_x\partial_y^2u\right)+\partial_yu\left(\partial_y^3u+\partial_y\partial_x^2u\right).\end{aligned}\tag{4.13}$$

Subsequently, we can derive nonlinear weights that satisfy the following relationship in smooth regions:

$$\omega_o=\gamma_o+\mathcal{O}(h^2),\quad o=s,f.\tag{4.14}$$

Hence we find that $u^{\text{WHC-4}}_{(i+\frac{1}{2},-),j+G}$ provides a fourth order accurate approximation to the exact value $u(x_{i+\frac{1}{2}},y_{j+G})$, as shown in the equation below:

$$u^{\text{WHC-4}}_{(i+\frac{1}{2},-),j+G}=u^f_{(i+\frac{1}{2},-),j+G}+\mathcal{O}(h^4)=u(x_{i+\frac{1}{2}},y_{j+G})+\mathcal{O}(h^4).\tag{4.15}$$

The validity of the first equality can be substantiated by the subsequent equation:

$$u^{\text{WHC-4}}_{(i+\frac{1}{2},-),j+G}=u^f_{(i+\frac{1}{2},-),j+G}+\frac{\omega_f-\gamma_f}{\gamma_f}\left(u^f_{(i+\frac{1}{2},-),j+G}-u^s_{(i+\frac{1}{2},-),j+G}\right)=u^f_{(i+\frac{1}{2},-),j+G}+\mathcal{O}(h^4).\tag{4.16}$$

In the vicinity of discontinuities, ω_s approximates to 1, thereby allowing the lower construction to take effect and prevent oscillations:

$$\omega_s=1-\mathcal{O}(h^4),\quad \omega_f=\mathcal{O}(h^4).\tag{4.17}$$

In cases where $k>2$, such as when $k=4$ for the eighth order accuracy, minor modifications to the existing reconstruction are required:

- Substitute $p^f(x,y)$ with the polynomial $p^e(x,y)$, which is derived from the eighth order reconstruction.
- Recompute the smoothness indicators.

- Adjust the power q in (4.7) to 3.

Thus we have obtained two-dimensional weighted Hermite reconstructions of the fourth and eighth order accuracy. These reconstructions are referred to as WHC-4 and WHC-8, respectively.

4.2 Hybrid choice of Hermite reconstructions

In the weighted Hermite reconstruction, two candidate reconstructions are computed and combined in a convex manner. However, in smooth regions, only the computation of the higher order reconstruction holds significance. As a result, a hybrid choice strategy, based on the performance analysis of the weighted reconstruction, could be a more effective approach. This strategy, which was first proposed in [21], has been widely applied in various contexts, as exemplified by [22].

We revisit (4.6):

$$u^{\text{WHC-4}}_{(i+\frac{1}{2},-),j+G}=\frac{\omega_f}{\gamma_f}u^f_{(i+\frac{1}{2},-),j+G}+\left(1-\frac{\omega_f}{\gamma_f}\right)u^s_{(i+\frac{1}{2},-),j+G}.$$

We observe that the coefficient of the first term, ω_f/γ_f, tends towards 1 in regions of smoothness, while this coefficient tends towards 0 in the vicinity of discontinuities. Hence we apply a truncation function to (4.6) to obtain our hybrid reconstruction:

$$u^{\text{HHC-4}}_{(i+\frac{1}{2},-),j+G}=\delta\left(\frac{\omega_f}{\gamma_f}\right)u^f_{(i+\frac{1}{2},-),j+G}+\left(1-\delta\left(\frac{\omega_f}{\gamma_f}\right)\right)u^s_{(i+\frac{1}{2},-),j+G}. \tag{4.18}$$

Here, the superscript "HHC" stands for "Hybrid Hermite Construction", and δ is the truncation function defined as

$$\delta(\xi)=\begin{cases}1, & \xi>C/\gamma_f,\\ 0, & \xi\leqslant C/\gamma_f,\end{cases} \tag{4.19}$$

where C is a threshold that lies within the interval $(0,\gamma_f)$. Then (4.18) is equivalent to

$$u^{\text{HHC-4}}_{(i+\frac{1}{2},-),j+G}=\begin{cases}u^f_{(i+\frac{1}{2},-),j+G}, & \omega_f>C,\\ u^s_{(i+\frac{1}{2},-),j+G}, & \omega_f\leqslant C.\end{cases} \tag{4.20}$$

Similar to the one-dimensional case, we can establish a threshold $\bar{\vartheta}$ that is solely dependent on the threshold C and the linear weights γ_s and γ_f. This results in the condition $\omega_f>C$ being equivalent to $\beta_f+\varepsilon<\bar{\vartheta}(\beta_s+\varepsilon)$, and (4.20) is equivalent to

$$u^{\text{HHC-4}}_{(i+\frac{1}{2},-),j+G}=\begin{cases}u^f_{(i+\frac{1}{2},-),j+G}, & \beta_f+\varepsilon<\bar{\vartheta}(\beta_s+\varepsilon),\\ u^s_{(i+\frac{1}{2},-),j+G}, & \beta_f+\varepsilon\geqslant\bar{\vartheta}(\beta_s+\varepsilon).\end{cases} \tag{4.21}$$

This is our final HHC-4 reconstruction. Compared to the WHC reconstruction, it eliminates the need for calculating nonlinear weights ω_s and ω_f.

Remark 4.1. We note that only the value of the threshold $\bar{\vartheta}$ needs to be determined, given the direct relationship between $\bar{\vartheta}$ and C.

In fact, the inequality in (4.21) can be interpreted as a comparison between ϑ and the threshold $\bar{\vartheta}$, where

$$\vartheta=\frac{\beta_f+\varepsilon}{\beta_s+\varepsilon}. \tag{4.22}$$

Upon careful analysis, we find that ϑ is close to 1 in smooth regions,

$$\vartheta=\frac{\beta_f+\varepsilon}{\beta_s+\varepsilon}=1+\frac{\beta_f-\beta_s}{\beta_s+\varepsilon}=1+\mathcal{O}(h), \tag{4.23}$$

while in the vicinity of discontinuities, it is a relatively large number,

$$\vartheta=\frac{\beta_f+\varepsilon}{\beta_s+\varepsilon}=\mathcal{O}(h^{-2}), \tag{4.24}$$

where the coefficients of h and h^{-2} vary with the problem. We can provide an empirical parameter range, $\bar{\vartheta}\in(5,50)$, and we most recommend $\bar{\vartheta}=20$.

In the case of $k=4$, corresponding to the eighth order accuracy, the recommended threshold $\bar{\vartheta}$ is different from the case $k=2$. We propose that $\bar{\vartheta}$ should fall within the empirical range of $(50000,500000)$, with a strong recommendation for $\bar{\vartheta}=200000$. Apart from this, the eighth and fourth order HHC reconstructions are similar.

We have successfully derived two-dimensional hybrid Hermite reconstructions of the fourth and eighth order accuracy, referred to as HHC-4 and HHC-8 respectively.

We have the following observations regarding the WHC-4 and HHC-4 reconstructions:

- The HHC-4 reconstruction selects among candidate stencils by conducting a straightforward comparison of smoothness indicators, making it more efficient than the WHC-4 reconstruction.
- In the vicinity of discontinuities, the HHC-4 reconstruction fully adopts the GRP reconstruction, which exhibits robust numerical performance in resolving discontinuities.
- In regions of high smoothness, the HHC-4 reconstruction exclusively employs the HC-4 reconstruction, which has better accuracy.

4.3 The compactness of our schemes

We substitute the reconstruction $\mathcal{R}$ in (2.3) with the WHC-4 reconstruction in (4.6) or HHC-4 reconstruction in (4.21), substitute the Lax-Wendroff type flow solver $\mathcal{G}$ in (2.6) with the GRP solver [15], and obtain the corresponding compact Hermite schemes, such as the WHC-4 and HHC-4 schemes. The WHC-8 and HHC-8 schemes are similar.

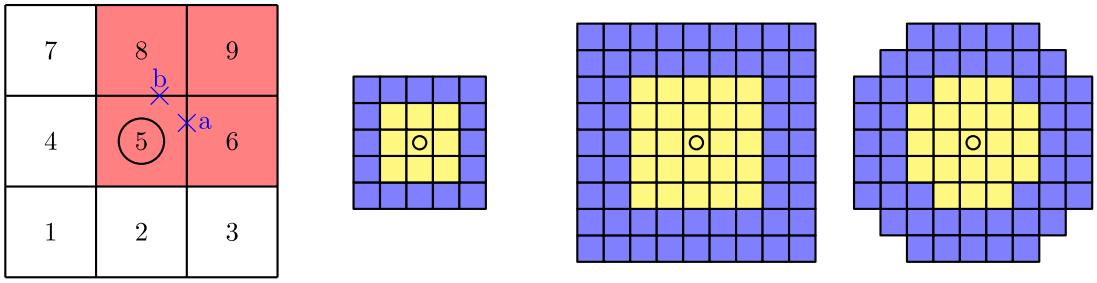

Figure 2: The diagrammatic presentation for dependency regions. The figures show cells in time level $t=t^n$. The cell marked with ○ is I_{ij}. The red cells represent the dependency region of the numerical flux $\hat{f}^*_{i+\frac{1}{2},j+G}$ and the interface value $\hat{\boldsymbol{u}}^{n+\frac{1}{2}}_{i+\frac{1}{2},j+G}$. The yellow cells represent the dependency region of the average data $\bar{\boldsymbol{u}}^{n+\frac{1}{2}}_{ij}$, $\bar{\boldsymbol{v}}^{n+\frac{1}{2}}_{ij}$, and $\bar{\boldsymbol{w}}^{n+\frac{1}{2}}_{ij}$ in time level $t=t^{n+\frac{1}{2}}$, and the combination of the yellow and blue cells represent the dependency region of the average data in time level $t=t^{n+1}$. (a) The dependency region of the numerical flux of the WHC-4 and HHC-4 schemes. (b) The dependency region of the WHC-4 and HHC-4 schemes. (c) The dependency region of the S2O4-HWENO5 scheme in [13]. (d) The dependency region of the S2O4-HWENO4 scheme in [5].

We would like to discuss the concept of compactness. The fewer cells a scheme depends on at time level $t=t^n$ for each cell at time level $t=t^{n+1}$, the more compact the scheme is. Consider our WHC-4 scheme as an example. The reconstructed values $\boldsymbol{u}^n_{(i+\frac{1}{2},\pm),j+G}$, $(\partial_x\boldsymbol{u})^n_{(i+\frac{1}{2},\pm),j+G}$, $(\partial_y\boldsymbol{u})^n_{(i+\frac{1}{2},\pm),j+G}$, $(\partial^2_x\boldsymbol{u})^n_{(i+\frac{1}{2},\pm),j+G}$, $(\partial_x\partial_y\boldsymbol{u})^n_{(i+\frac{1}{2},\pm),j+G}$ and $(\partial^2_y\boldsymbol{u})^n_{(i+\frac{1}{2},\pm),j+G}$, on both sides of Gaussian point "a", as shown in Fig. 2(a), depend on four cells #5, #6, #8, and #9 at time level $t=t^n$. The same situation applies to the Gaussian point "b". Consequently, the numerical flux $\hat{\boldsymbol{f}}^*_{i+\frac{1}{2},j+G}$ and the interface value $\hat{\boldsymbol{u}}^{n+\frac{1}{2}}_{i+\frac{1}{2},j+G}$ at this Gaussian point depend on these four cells. Similarly, the numerical flux and the interface value at the eight Gaussian points of cell I_{ij} depend on nine cells, #1 to #9. Therefore, the average data $\bar{\boldsymbol{u}}^{n+\frac{1}{2}}_{ij}$, $\bar{\boldsymbol{v}}^{n+\frac{1}{2}}_{ij}$, and $\bar{\boldsymbol{w}}^{n+\frac{1}{2}}_{ij}$ depend on nine cells at time level $t=t^n$, which are the yellow cells in Fig. 2(b).

Furthermore, the average data at time level $t=t^{n+1}$ depend on 25 cells at time level $t=t^n$, which are the yellow and blue cells in Fig. 2(b). A similar situation applies to our HHC-4 scheme. As a comparison, the S2O4-HWENO5 scheme in [13], which is computed dimension by dimension, depends on 81 cells at time level $t=t^n$ to obtain average data at time level $t=t^{n+1}$, as shown in Fig. 2(c). If one chooses the genuinely two-dimensional HWENO4 reconstruction in [5] combined with the S_2O_4 framework, the average data at time level $t=t^{n+1}$ depends on 69 cells at time level $t=t^n$, as shown in Fig. 2(d).

5 Numerical examples

In this section, we evaluate the performance of the schemes obtained in this paper with the two-dimensional Euler system. The system is described by the following equations:

$$\begin{cases} \partial_t \boldsymbol{u}+\partial_x \boldsymbol{f}(\boldsymbol{u})+\partial_y \boldsymbol{g}(\boldsymbol{u})=0, \\ \boldsymbol{u}=(\rho,\rho u,\rho v,\rho E)^\top, \\ \boldsymbol{f}=(\rho u,\rho u^2+p,\rho uv,u(\rho E+p))^\top, \\ \boldsymbol{g}=(\rho v,\rho uv,\rho v^2+p,v(\rho E+p))^\top, \end{cases} \tag{5.1}$$

where ρ, u, v, E, and p are the density, velocity components, total energy, and pressure, respectively. The thermodynamic variables satisfy the state equation $p=(\gamma-1)(\rho E-\frac{1}{2}\rho(u^2+v^2))$, where γ is the adiabatic index. The value of γ is typically set to 1.4, but it may vary depending on specific conditions.

5.1 The fourth order compact Hermite schemes

We first perform the tests on our fourth order compact Hermite schemes, the WHC-4 and HHC-4 schemes, the CFL number is set to be 0.6 and the threshold $\bar{\vartheta}$ is set to 20.

Example 5.1 (Linear continuous problem)**.** This test case is designed for the purpose of verifying accuracy. The initial conditions for the Euler system are established as

$$(\rho,u,v,p)(x,y,0)=(1+0.2\sin(\pi(x+y)),0.7,0.3,1). \tag{5.2}$$

The computational domain is defined as $[-1,1]\times[-1,1]$. Uniform meshes ($h_x=h_y=h$) and periodic boundaries are applied. The exact solution is a shift of the initial values

$$\boldsymbol{u}(x,y,t)=\boldsymbol{u}(x-0.7t,y-0.3t,0). \tag{5.3}$$

The results corresponding to the terminal time $t^{tem}=2$ are presented in Table 2. It can be observed that both schemes achieve their designed accuracy.

Example 5.2 (Nonlinear continuous problem)**.** This test case further verifies the accuracy of the schemes. If there are concerns that Example 5.1 is linearly degenerate and does not test the impact of the equation's nonlinearity on the accuracy of the scheme, this test case, which is derived from [23], can address those concerns. The initial conditions are set as

$$\begin{aligned} &\rho(x,y,0)=\frac{1+0.2\sin(0.5(x+y))}{\sqrt{6}}, \\ &u(x,y,0)=v(x,y,0)=\sqrt{\frac{\gamma}{2}}\rho(x,y,0), \\ &p(x,y,0)=\rho(x,y,0)^\gamma. \end{aligned} \tag{5.4}$$

Table 2: The L^1 and L^∞ errors of the density and the orders, of the linear continuous problem in Example 5.1. The results are shown at $t^{tem}=2$.

CFL	h	WHC-4				HHC-4			
		L^1-error	Order	L^∞-error	Order	L^1-error	Order	L^∞-error	Order
0.6	2/10	3.840E-3		5.932E-3		3.840E-3		5.933E-3	
0.6	2/20	2.544E-4	3.916	3.939E-4	3.913	2.544E-4	3.916	3.939E-4	3.913
0.6	2/40	1.594E-5	3.997	2.494E-5	3.981	1.594E-5	3.997	2.494E-5	3.981
0.6	2/80	9.964E-7	4.000	1.564E-6	3.995	9.963E-7	4.000	1.564E-6	3.996
0.6	2/160	6.228E-8	4.000	9.781E-8	3.999	6.227E-8	4.000	9.780E-8	3.999
0.6	2/320	3.892E-9	4.000	6.137E-9	3.994	3.892E-9	4.000	6.136E-9	3.994

Table 3: The L^1 and L^∞ errors of the density and the orders of the nonlinear continuous problem in Example 5.2. The results are shown at $t^{tem}=2$.

CFL	h	WHC-4				HHC-4			
		L^1-error	Order	L^∞-error	Order	L^1-error	Order	L^∞-error	Order
0.6	$4\pi/150$	2.109E-8		1.119E-7		2.109E-8		1.119E-7	
0.6	$4\pi/200$	6.844E-9	3.912	3.010E-8	4.566	6.844E-9	3.912	3.010E-8	4.566
0.6	$4\pi/250$	2.805E-9	3.997	1.236E-8	3.990	2.805E-9	3.997	1.236E-8	3.990
0.6	$4\pi/300$	1.352E-9	4.003	5.972E-9	3.988	1.352E-9	4.003	5.972E-9	3.988
0.6	$4\pi/350$	7.293E-10	4.003	3.234E-9	3.978	7.293E-10	4.003	3.234E-9	3.978
0.6	$4\pi/400$	4.274E-10	4.003	1.913E-9	3.932	4.274E-10	4.003	1.913E-9	3.932

The computational domain is defined as $[0,4\pi]\times[0,4\pi]$, and the same uniform meshes and periodic boundaries as in Example 5.1 are applied. The adiabatic index γ is set to 3. The exact solution can be obtained by solving the Burgers equation for $\mu(x,y,t)$:

$$\partial_t\mu+\frac{1}{2}\partial_x\left(\mu^2\right)+\frac{1}{2}\partial_y\left(\mu^2\right)=0,\quad \mu(x,y,0)=1+0.2\sin(0.5(x+y)). \tag{5.5}$$

The exact solution can then be expressed as

$$\begin{aligned}&\rho(x,y,t)=\frac{\mu(x,y,t)}{\sqrt{6}},\\ &u(x,y,t)=v(x,y,t)=\sqrt{\frac{\gamma}{2}}\rho(x,y,t),\\ &p(x,y,t)=\rho(x,y,t)^\gamma.\end{aligned} \tag{5.6}$$

The results corresponding to the time $t^{tem}=1$ are presented in Table 3. It can be observed that each scheme achieves its designed accuracy, even in the presence of a nonlinear flow field.

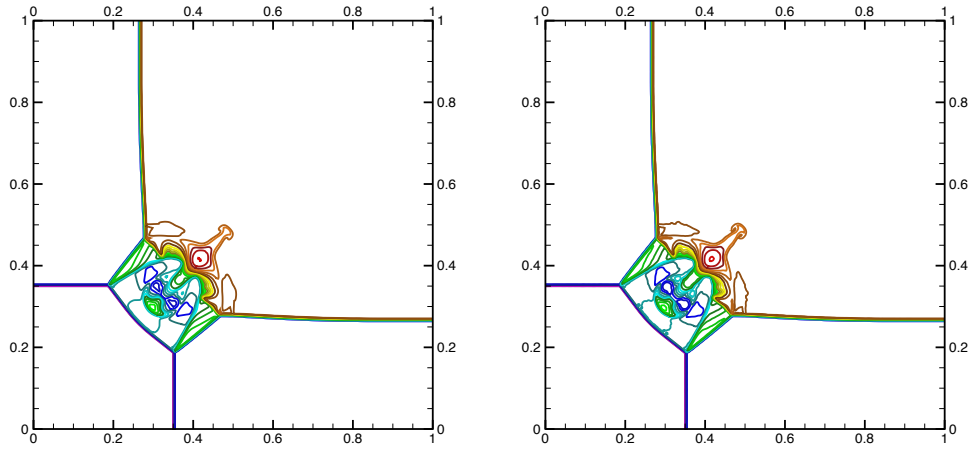

(a) WHC-4 (b) HHC-4

Figure 3: The density counters of the first 2D Riemann problem in Example 5.3. The results are shown at $t^{tem}=0.35$. 400×400 cells are used.

Example 5.3 (Riemann problem 1)**.** After verifying the accuracy of the schemes, we proceed to test an example involving discontinuities, specifically one that includes the interaction of four shock waves as presented in [24]. The computational domain is $[0,1]\times[0,1]$, with the initial conditions given by

$$(\rho,u,v,p)(x,y)=\begin{cases}(1.5,0,0,1.5), & \text{for } x>0.5 \text{ and } y>0.5,\\ (0.532,1.206,0,0.3), & \text{for } x<0.5 \text{ and } y>0.5,\\ (0.138,1.206,1.206,0.029), & \text{for } x<0.5 \text{ and } y<0.5,\\ (0.532,0,1.206,0.3), & \text{for } x>0.5 \text{ and } y<0.5.\end{cases} \tag{5.7}$$

The results at $t^{tem}=0.35$ are shown in Fig. 3. We have observed that both schemes are proficient in capturing small structures. The HHC-4 scheme performs slightly better than the WHC-4 scheme, albeit with a slight increase in oscillation.

Example 5.4 (Riemann problem 2)**.** This is an example from [24] involving the interaction of four rarefaction waves. The computational domain is $[0,1]\times[0,1]$, with the initial conditions given by

$$(\rho,u,v,p)(x,y)=\begin{cases}(1,0,0,1), & \text{for } x>0.5 \text{ and } y>0.5,\\ (0.52,-0.726,0,0.4), & \text{for } x<0.5 \text{ and } y>0.5,\\ (1,-0.726,-0.726,1), & \text{for } x<0.5 \text{ and } y<0.5,\\ (0.52,0,-0.726,0.4), & \text{for } x>0.5 \text{ and } y<0.5.\end{cases} \tag{5.8}$$

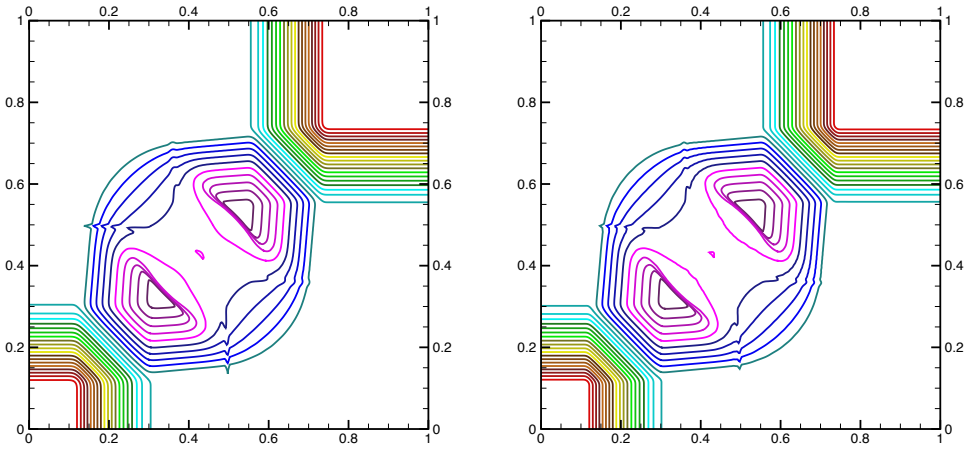

(a) WHC-4 (b) HHC-4

Figure 4: The density counters of the second 2D Riemann problem in Example 5.4. The results are shown at $t^{tem}=0.2$. 400×400 cells are used.

The results at $t^{tem}=0.2$ are shown in Fig. 4. It is evident that all these schemes perform effectively, and the conclusions drawn from the inter-comparisons are similar to the previous example.

Example 5.5 (Riemann problem 3)**.** Next, we test an example from [24] involving the interaction of rarefaction waves and vortex-sheets. The computational domain is also $[0,1]\times[0,1]$, with the initial conditions given by

$$(\rho,u,v,p)(x,y)=\begin{cases}(1,0.1,0.1,1), & \text{for } x>0.5 \text{ and } y>0.5,\\ (0.52,-0.626,0.1,0.4), & \text{for } x<0.5 \text{ and } y>0.5,\\ (0.8,0.1,0.1,0.4), & \text{for } x<0.5 \text{ and } y<0.5,\\ (0.52,0.1,-0.626,0.4), & \text{for } x>0.5 \text{ and } y<0.5.\end{cases} \tag{5.9}$$

The results at $t^{tem}=0.3$ are shown in Fig. 5. We can see that both schemes are able to depict the interaction between rarefaction waves and vortex-sheets well. The HHC-4 scheme performs better in capturing small vortices than the WHC-4 scheme, albeit at the cost of introducing marginally oscillations.

Example 5.6 (Double Mach reflection problem)**.** This is a classic test case. An oblique shock wave hits a reflective boundary, with the post-shock state being $\boldsymbol{u}_L$ and the pre-shock state being $\boldsymbol{u}_R$.

$$\begin{aligned}&\boldsymbol{u}_L=(\rho_L,u_L,v_L,p_L)=(8,4.125\sqrt{3},-4.125,116.5),\\ &\boldsymbol{u}_R=(\rho_R,u_R,v_R,p_R)=(1.4,0,0,1).\end{aligned} \tag{5.10}$$

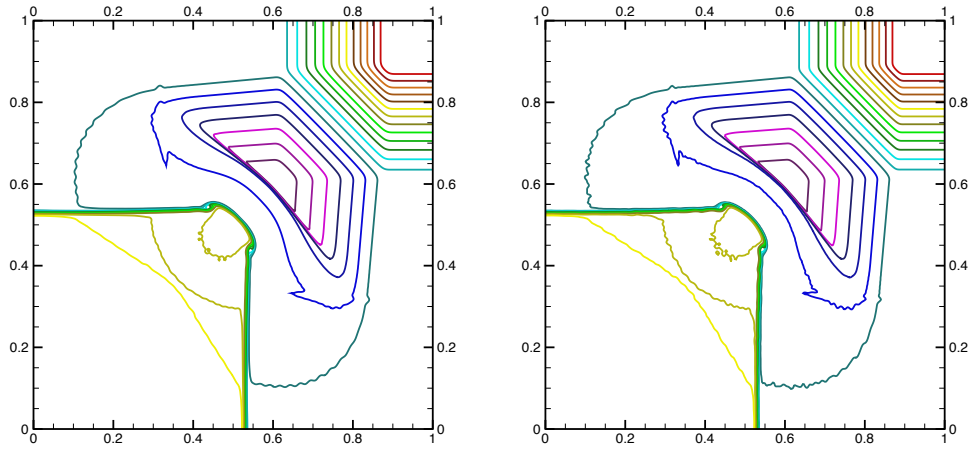

(a) WHC-4 (b) HHC-4

Figure 5: The density counters of the third 2D Riemann problem in Example 5.5. The results are shown at $t^{tem}=0.3$. 400×400 cells are used.

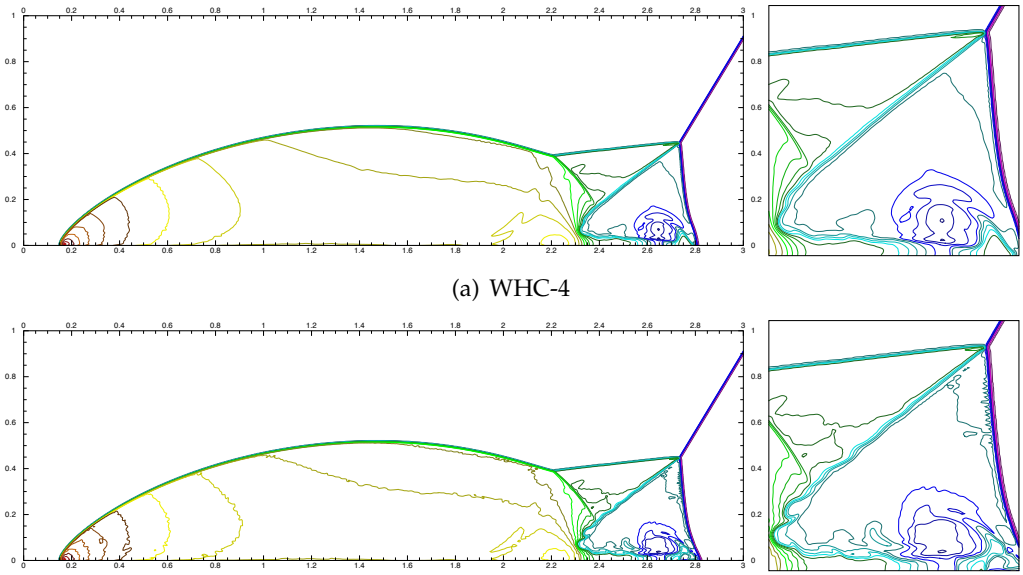

(a) WHC-4

(b) HHC-4

Figure 6: The density counters of the double Mach problem in Example 5.6. The results are shown at $t^{tem}=0.2$. 1440×360 cells are used.

The Mach number is 10. The computational domain is $[0,4]\times[0,1]$. At $t^{tem}=0.2$, the results for the domain $[0,3]\times[0,1]$ are shown in Fig. 6. We can see that both schemes have done a good job of depicting the interaction between shock waves and reflection bound-

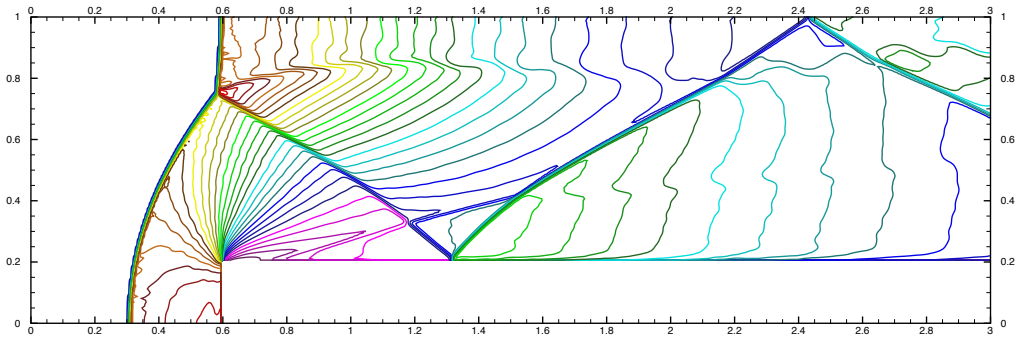

(a) WHC-4

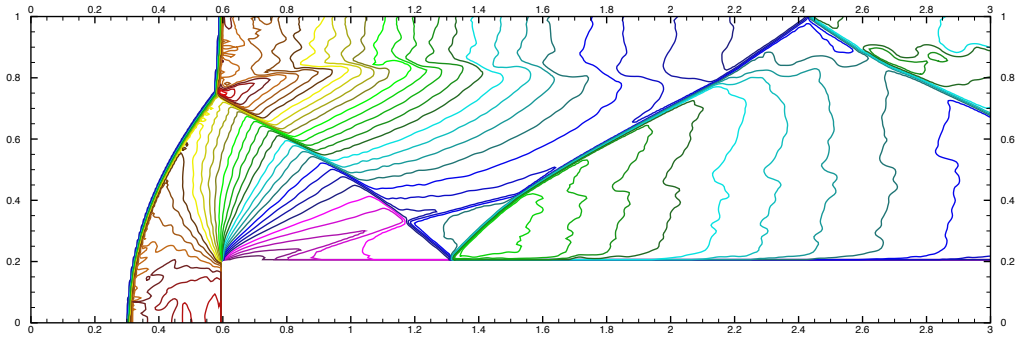

(b) HHC-4

Figure 7: The density counters of the front step problem in Example 5.7. The results are shown at $t^{tem}=4$. 480×160 cells are used.

aries, providing a clear position of the Mach stem. The HHC-4 scheme captures more small vortex structures than the WHC-4 scheme, but it also introduces slightly larger oscillations.

Example 5.7 (Forward step problem)**.** The forward step problem is a classic test case that describes a wind tunnel with a step, initially filled with a uniform Mach 3 flow. The state of the flow is given by

$$(\rho,u,v,p)=(1.4,3,0,1). \tag{5.11}$$

The walls of the wind tunnel serve as reflective boundaries, while the left and right sides serve as inflow and outflow boundaries, respectively. At the corner of the step, we have adopted the same technique as that in pp. 131–132 of [25] to enhance the computational results. The results at $t^{tem}=4$ are shown in Fig. 7. It is evident that both schemes have done a good job of depicting the impact of the step on the stable inflow, capturing clear flow structures. The oscillations introduced by the HHC-4 schemes is slightly larger than that of the WHC-4 scheme.

5.2 The eighth order compact Hermite schemes

Although the eighth-order schemes are by-products of our study, we will also briefly test their performance. The CFL number is set to be 0.5 and the threshold $\bar{\vartheta}$ is set to 200000. First we consider the continuous examples, Examples 5.1 and 5.2. For the schemes such as the WHC-8 scheme, the spatial order is higher than the temporal order, and we take the same treatments as that in [14] to obtain the order of reconstruction. The findings presented in Tables 4 and 5 demonstrate that each scheme successfully achieves its designed accuracy. When comparing the fourth-order and eighth-order accurate schemes, it is suitable to focus on which has a lower CPU Time for the same error. As shown in Fig. 8, we can observe that the eighth-order accurate scheme exhibits superior time efficiency.

As for the discontinuous case, we tested the Riemann problem, Examples 5.3 to 5.5, and obtained the results shown in Fig. 9. The performance of the two eighth-order schemes, despite using fewer cells, is comparable to that of the two fourth-order schemes.

Table 4: The L^1 and L^∞ errors of the density and the orders of the linear continuous problem in Example 5.1. The results are shown at $t^{tem}=2$.

CFL	h	WHC-8				HHC-8			
		L^1-error	Order	L^∞-error	Order	L^1-error	Order	L^∞-error	Order
0.500	2/10	1.659E-5		2.568E-5		1.661E-5		2.566E-5	
0.250	2/20	8.084E-8	7.681	1.278E-7	7.651	8.135E-8	7.673	1.258E-7	7.672
0.500	2/20	1.610E-7		2.502E-7		1.610E-7		2.523E-7	
0.250	2/40	6.764E-10	7.895	1.081E-9	7.854	6.745E-10	7.899	1.057E-9	7.900
0.500	2/40	4.929E-9		7.619E-9		4.930E-9		7.756E-9	
0.333	2/60	1.973E-10	7.936	3.016E-10	7.965	1.975E-10	7.935	3.110E-10	7.933
0.500	2/60	6.574E-10		9.969E-10		6.587E-10		1.035E-9	
0.375	2/80	6.715E-11	7.930	1.105E-10	7.647	6.733E-11	7.928	1.067E-10	7.898

Table 5: The L^1 and L^∞ errors of the density and the orders of the nonlinear continuous problem in Example 5.2. The results are shown at $t^{tem}=2$.

CFL	h	WHC-8				HHC-8			
		L^1-error	Order	L^∞-error	Order	L^1-error	Order	L^∞-error	Order
0.500	$4\pi/100$	8.826E-10		4.698E-9		8.826E-10		4.698E-9	
0.417	$4\pi/120$	2.243E-10	7.514	1.203E-9	7.471	2.243E-10	7.514	1.203E-9	7.471
0.500	$4\pi/120$	3.478E-10		1.844E-9		3.478E-10		1.844E-9	
0.429	$4\pi/140$	1.092E-10	7.516	5.926E-10	7.363	1.092E-10	7.516	5.926E-10	7.363
0.500	$4\pi/140$	1.607E-10		8.366E-10		1.607E-10		8.366E-10	
0.438	$4\pi/160$	5.852E-11	7.565	3.173E-10	7.261	5.852E-11	7.565	3.173E-10	7.261
0.500	$4\pi/160$	8.300E-11		4.180E-10		8.300E-11		4.180E-10	
0.444	$4\pi/180$	3.405E-11	7.566	1.833E-10	7.000	3.405E-11	7.566	1.833E-10	7.000

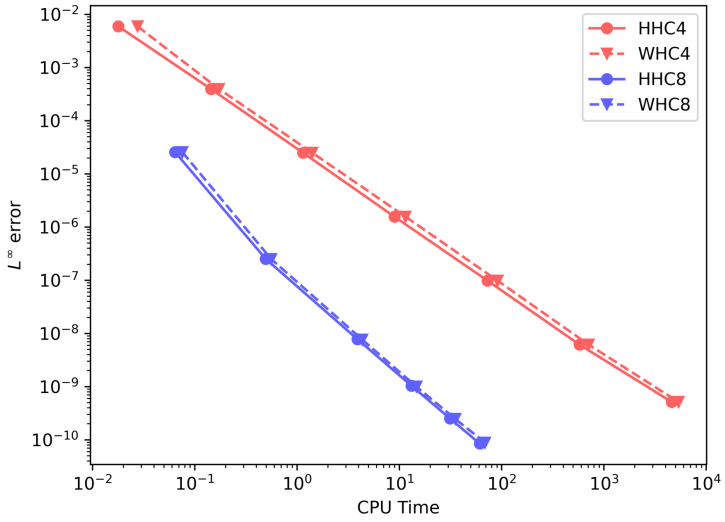

Figure 8: The relationship between CPU Time and the L^∞ error of the density in Example 5.1.

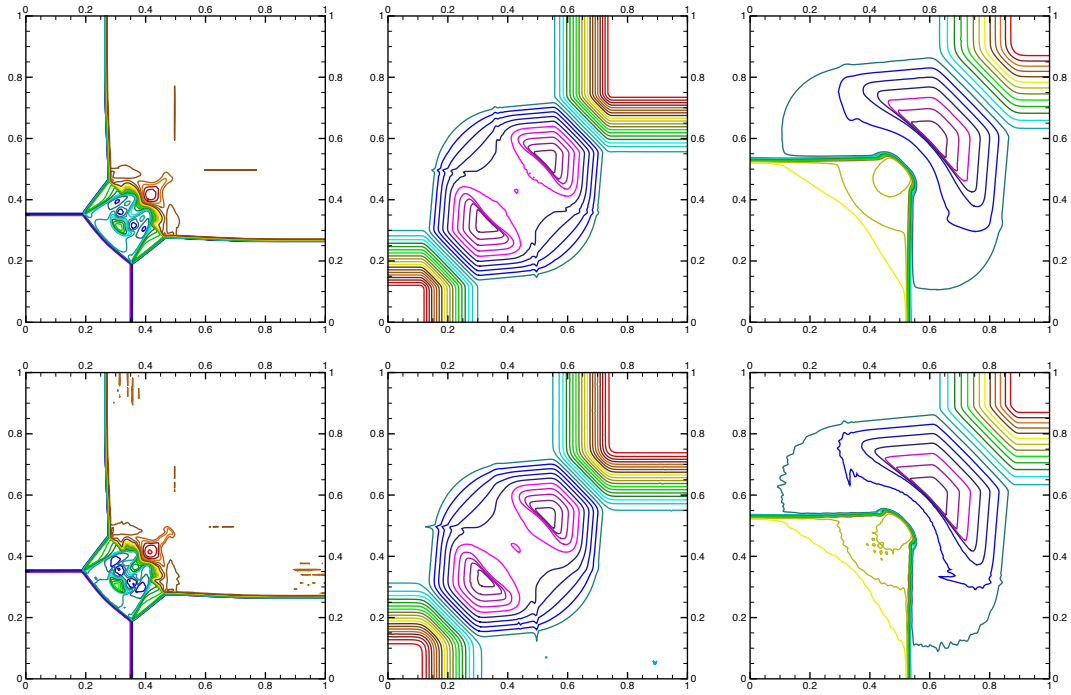

Figure 9: The density counters of the second 2D Riemann problem. 300×300 cells are used. Top: WHC-8 scheme, bottom: HHC-8 scheme, left: Example 5.3, $t^{tem}=0.35$, middle: Example 5.4, $t^{tem}=0.2$, right Example 5.5, $t^{tem}=0.3$.

6 Concluding remarks

The original two-dimensional S2O4-HWENO5 scheme in [13] is based on dimension-by-dimensional HWENO5 and WENO5 reconstructions and the GRP solver. In order to further improve the compactness and efficiency of the numerical scheme, we design a new type of S_2O_4 finite volume scheme, which is based on nonlinear compact Hermite reconstructions and the GRP solver, and uses the improved S_2O_4 framework. These nonlinear compact Hermite reconstructions apply WENO technique or hybrid choice strategy to avoid oscillations near discontinuities. The new two-stage fourth order numerical schemes are high-order, stable, compact, efficient and essentially non-oscillatory. We note that the reconstruction designed in this paper is genuinely two-dimensional, which can be potentially extended to unstructured meshes. Afterwards, the above reconstructions and the corresponding numerical schemes are extended to eighth-order accuracy in space, and potentially to any $2k$-order accuracy. A large number of numerical examples are provided to demonstrate the desirable properties of the high order Hermite schemes. The design of the Hermite reconstruction on unstructured meshes, the three-dimensional Hermite reconstruction, and more studies on the proof of stability of the schemes proposed in this paper and beyond, are left for our future work.

Acknowledgments

J. Cheng is supported by NSFC grant 12031001 and National Key R&D Program of China No. 2022YFA1004500. C.-W. Shu is supported by NSF grant DMS-2309249.

A The details for obtaining the second derivative $\left(\partial_t^2 \boldsymbol{u}\right)^{n,+}_{i+\frac{1}{2},j\pm G}$

The second derivative $\left(\partial_t^2 \boldsymbol{u}\right)^{n,+}_{i+\frac{1}{2},j+G}$ can be obtained by taking derivatives of the PDE, once we have obtained the following values at the Gaussian point $(x_{i+\frac{1}{2}}, y_{j+G})$,

$$\boldsymbol{u}_{\pm},\ \boldsymbol{u}^{+},\ \left(\partial_x \boldsymbol{u}\right)_{\pm},\ \left(\partial_y \boldsymbol{u}\right)_{\pm},\ \left(\partial_t \boldsymbol{u}\right)^{+},\ \left(\partial_x^2 \boldsymbol{u}\right)_{\pm},\ \left(\partial_x \partial_y \boldsymbol{u}\right)_{\pm},\ \left(\partial_y^2 \boldsymbol{u}\right)_{\pm},$$

where the subscripts are simplified, such as $\boldsymbol{u}_{\pm}$ represents $\boldsymbol{u}^{n}_{(i+\frac{1}{2},\pm),j+G}$ and $\boldsymbol{u}^{+}$ represents $\boldsymbol{u}^{n,+}_{i+\frac{1}{2},j+G}$. Note that the second derivative $\left(\partial_t^2 \boldsymbol{u}\right)^{+}$ here is only for ensuring accuracy, hence it should be bounded and $\frac{\tau^2}{8}\left(\partial_t^2 \boldsymbol{u}\right)^{+} = \mathcal{O}(\tau^2)$ when the solution is near discontinuities. This condition allows the improved S_2O_4 framework to converge towards the original S_2O_4 framework, thereby maintains similar performance. Fortunately, the HWENO reconstruction can achieve this condition automatically by mainly adopting the polynomial of at most first degree with minmod limiter in the vicinity of discontinuities. Consequently, the values of second spatial derivatives approach zero and the values of first

spatial derivatives are both bounded. By applying the following formula, specifically (A.1) to (A.3), we can confirm that the value of $\left(\partial_t^2 \boldsymbol{u}\right)^+$ is indeed bounded. Next, we discuss the case when the solution is in regions of smoothness. Spatial derivatives are approximated by arithmetic mean:

$$\left(\partial_x^{d_1}\partial_y^{d_2}\boldsymbol{u}\right)^+ = \frac{1}{2}\left(\partial_x^{d_1}\partial_y^{d_2}\boldsymbol{u}\right)_+ + \frac{1}{2}\left(\partial_x^{d_1}\partial_y^{d_2}\boldsymbol{u}\right)_-, \quad d_1+d_2=1,2, \tag{A.1}$$

and we have

$$\begin{aligned}\left(\partial_t^2\boldsymbol{u}\right)^+ =& -\partial_t\partial_x\left(\boldsymbol{f}(\boldsymbol{u}^+)\right)-\partial_t\partial_y\left(\boldsymbol{g}(\boldsymbol{u}^+)\right)\\ =& -\partial_x\left(\frac{\partial \boldsymbol{f}}{\partial \boldsymbol{u}}(\boldsymbol{u}^+)\left(\partial_t\boldsymbol{u}\right)^+\right)-\partial_y\left(\frac{\partial \boldsymbol{g}}{\partial \boldsymbol{u}}(\boldsymbol{u}^+)\left(\partial_t\boldsymbol{u}\right)^+\right)\\ =& -\frac{\partial^2 \boldsymbol{f}}{\partial \boldsymbol{u}^2}(\boldsymbol{u}^+)\left(\partial_x\boldsymbol{u}\right)^+\left(\partial_t\boldsymbol{u}\right)^+-\frac{\partial \boldsymbol{f}}{\partial \boldsymbol{u}}(\boldsymbol{u}^+)\left(\partial_x\partial_t\boldsymbol{u}\right)^+\\ &-\frac{\partial^2 \boldsymbol{g}}{\partial \boldsymbol{u}^2}(\boldsymbol{u}^+)\left(\partial_y\boldsymbol{u}\right)^+\left(\partial_t\boldsymbol{u}\right)^+-\frac{\partial \boldsymbol{g}}{\partial \boldsymbol{u}}(\boldsymbol{u}^+)\left(\partial_y\partial_t\boldsymbol{u}\right)^+.\end{aligned} \tag{A.2}$$

The only unknown values are spatial-temporal derivatives $\left(\partial_x\partial_t\boldsymbol{u}\right)^+$ and $\left(\partial_y\partial_t\boldsymbol{u}\right)^+$. The value of $\left(\partial_x\partial_t\boldsymbol{u}\right)^+$ can be obtained by

$$\begin{aligned}\left(\partial_x\partial_t\boldsymbol{u}\right)^+ =& -\partial_x\partial_x\left(\boldsymbol{f}(\boldsymbol{u}^+)\right)-\partial_x\partial_y\left(\boldsymbol{g}(\boldsymbol{u}^+)\right)\\ =& -\partial_x\left(\frac{\partial \boldsymbol{f}}{\partial \boldsymbol{u}}(\boldsymbol{u}^+)\left(\partial_x\boldsymbol{u}\right)^+\right)-\partial_y\left(\frac{\partial \boldsymbol{g}}{\partial \boldsymbol{u}}(\boldsymbol{u}^+)\left(\partial_x\boldsymbol{u}\right)^+\right)\\ =& -\frac{\partial^2 \boldsymbol{f}}{\partial \boldsymbol{u}^2}(\boldsymbol{u}^+)\left(\partial_x\boldsymbol{u}\right)^+\left(\partial_x\boldsymbol{u}\right)^+-\frac{\partial \boldsymbol{f}}{\partial \boldsymbol{u}}(\boldsymbol{u}^+)\left(\partial_x^2\boldsymbol{u}\right)^+\\ &-\frac{\partial^2 \boldsymbol{g}}{\partial \boldsymbol{u}^2}(\boldsymbol{u}^+)\left(\partial_y\boldsymbol{u}\right)^+\left(\partial_x\boldsymbol{u}\right)^+-\frac{\partial \boldsymbol{g}}{\partial \boldsymbol{u}}(\boldsymbol{u}^+)\left(\partial_x\partial_y\boldsymbol{u}\right)^+,\end{aligned} \tag{A.3}$$

and $\left(\partial_y\partial_t\boldsymbol{u}\right)^+$ is similar. Then the value of $\left(\partial_t^2\boldsymbol{u}\right)^+$, i.e. $\left(\partial_t^2\boldsymbol{u}\right)^{n,+}_{i+\frac{1}{2},j+G}$ is clear. The value of $\left(\partial_t^2\boldsymbol{u}\right)^{n,+}_{i+\frac{1}{2},j-G}$ is similar.

B The Taylor analysis of the improved and original S_2O_4 framework

First, we try to analysis the accuracy of the improved S_2O_4 framework. For simplicity, we just analyze the case of linear equation,

$$\partial_t u+\partial_x u+\partial_y u=0, \tag{B.1}$$

and take the uniform square meshes $h_x=h_y=h$. Assume that the Hermite reconstruction attains desired order, i.e., fourth order accurate approximation to $u(x,y,0)$ itself, third

order to its gradient and second order to its second derivatives. Then we have

$$\begin{aligned}
\mathbb{T}u^0_{(i+\frac{1}{2},\pm),j+G}&=\mathcal{O}(h^4), \qquad \mathbb{T}\left(\partial_x u\right)^0_{(i+\frac{1}{2},\pm),j+G}=\mathcal{O}(h^3),\\
\mathbb{T}\left(\partial_y u\right)^0_{(i+\frac{1}{2},\pm),j+G}&=\mathcal{O}(h^3), \qquad \mathbb{T}\left(\partial_x^2 u\right)^0_{(i+\frac{1}{2},\pm),j+G}=\mathcal{O}(h^2),\\
\mathbb{T}\left(\partial_x\partial_y u\right)^0_{(i+\frac{1}{2},\pm),j+G}&=\mathcal{O}(h^2), \qquad \mathbb{T}\left(\partial_y^2 u\right)^0_{(i+\frac{1}{2},\pm),j+G}=\mathcal{O}(h^2),
\end{aligned} \tag{B.2}$$

where $\mathbb{T}$ represents the truncation error, i.e., $\mathbb{T}u^0_{(i+\frac{1}{2},\pm),j+G}=u^0_{(i+\frac{1}{2},\pm),j+G}-u(x_{i+\frac{1}{2}},y_{j+G},0)$, $u(x,y,t)$ is the exact solution; and similarly for the gradients. Then we obtain

$$\begin{aligned}
\mathbb{T}\hat{f}^*_{i+\frac{1}{2},j+G}=&\mathbb{T}u^0_{(i+\frac{1}{2},-),j+G}+\frac{\tau}{4}\mathbb{T}\left(\partial_t f\right)^{0,+}_{i+\frac{1}{2},j+G}-\frac{\tau^2}{24}\partial_t^2 u(x_{i+\frac{1}{2}},y_{j+G},0)+\mathcal{O}(\tau^3),\\
\mathbb{T}\hat{u}^{\frac{1}{2}}_{i+\frac{1}{2},j+G}=&\mathbb{T}u^0_{(i+\frac{1}{2},-),j+G}+\frac{\tau}{2}\mathbb{T}\left(\partial_t u\right)^{0,+}_{i+\frac{1}{2},j+G}+\frac{\tau^2}{8}\mathbb{T}\left(\partial_t^2 u\right)^{0,+}_{i+\frac{1}{2},j+G}\\
&-\frac{\tau^3}{48}\partial_t^3 u(x_{i+\frac{1}{2}},y_{j+G},0)+\mathcal{O}(\tau^4),
\end{aligned} \tag{B.3}$$

where

$$\begin{aligned}
&\mathbb{T}\left(\partial_t f\right)^{0,+}_{i+\frac{1}{2},j+G}=\mathbb{T}\left(\partial_t u\right)^{0,+}_{i+\frac{1}{2},j+G}=-\mathbb{T}\left(\partial_x u\right)^0_{(i+\frac{1}{2},-),j+G}-\mathbb{T}\left(\partial_y u\right)^0_{(i+\frac{1}{2},-),j+G},\\
&\mathbb{T}\left(\partial_t^2 u\right)^{0,+}_{i+\frac{1}{2},j+G}=\mathbb{T}\left(\partial_x^2 u\right)^0_{(i+\frac{1}{2},-),j+G}+2\mathbb{T}\left(\partial_x\partial_y u\right)^0_{(i+\frac{1}{2},-),j+G}+\mathbb{T}\left(\partial_y^2 u\right)^0_{(i+\frac{1}{2},-),j+G}.
\end{aligned} \tag{B.4}$$

Note that $\mathbb{T}\hat{f}^*_{i+\frac{1}{2},j+G}$ represents the truncation error of the numerical flux to the exact flux $f^*_{i+\frac{1}{2},j+G}=\frac{2}{\tau}\int_0^{\frac{\tau}{2}} f(x_{i+\frac{1}{2}},y_{j+G},t)dt$. Subsequently, since the two-point Gaussian integral has fourth-order accuracy, we have

$$\begin{aligned}
\mathbb{T}\hat{f}^*_{i+\frac{1}{2},j}&=\frac{1}{2}\mathbb{T}\hat{f}^*_{i+\frac{1}{2},j-G}+\frac{1}{2}\mathbb{T}\hat{f}^*_{i+\frac{1}{2},j+G}+\mathcal{O}(h^4),\\
\mathbb{T}\hat{u}^{\frac{1}{2}}_{i+\frac{1}{2},j}&=\frac{1}{2}\mathbb{T}\hat{u}^{\frac{1}{2}}_{i+\frac{1}{2},j-G}+\frac{1}{2}\mathbb{T}\hat{u}^{\frac{1}{2}}_{i+\frac{1}{2},j+G}+\mathcal{O}(h^4).
\end{aligned} \tag{B.5}$$

Note that $\mathbb{T}\hat{f}^*_{i+\frac{1}{2},j}$ represents the truncation error of the numerical flux to the exact flux $f^*_{i+\frac{1}{2},j}=\frac{2}{\tau h_y}\int_0^{\frac{\tau}{2}}\int_{y_{j-\frac{1}{2}}}^{y_{j+\frac{1}{2}}} f(u(x_{i+\frac{1}{2}},y,t))dydt$, and $\mathbb{T}\hat{u}^{\frac{1}{2}}_{i+\frac{1}{2},j}$ represents the truncation error of the line average along the interface to the exact value $\frac{1}{h}\int_{y_{j-\frac{1}{2}}}^{y_{j+\frac{1}{2}}} u(x_{i+\frac{1}{2}},y,\frac{\tau}{2})dy$. In the y direction, $\hat{\boldsymbol{g}}^*_{i,j+\frac{1}{2}}$ and $\hat{\boldsymbol{u}}^{\frac{1}{2}}_{i,j+\frac{1}{2}}$ are analysed similarly. Hence at the first time-stage $t=\frac{\tau}{2}$, we have

estimates

$$\begin{aligned}
&\mathbb{T}\bar{u}_{ij}^{\frac{1}{2}}=\mathbb{T}\bar{u}_{ij}^{0}-\frac{\tau}{2h}\Big(\mathcal{O}(h^4)+\mathcal{O}(\tau h^3)+\mathcal{O}(\tau^2 h)+\mathcal{O}(\tau^3)\Big)=\mathcal{O}(h^3),\\
&\mathbb{T}\bar{v}_{ij}^{\frac{1}{2}}=\frac{1}{h}\Big(\mathcal{O}(h^4)+\mathcal{O}(\tau h^3)+\mathcal{O}(\tau^2 h^2)+\mathcal{O}(\tau^3 h)+\mathcal{O}(\tau^4)\Big)=\mathcal{O}(h^3),\\
&\mathbb{T}\bar{w}_{ij}^{\frac{1}{2}}=\frac{1}{h}\Big(\mathcal{O}(h^4)+\mathcal{O}(\tau h^3)+\mathcal{O}(\tau^2 h^2)+\mathcal{O}(\tau^3 h)+\mathcal{O}(\tau^4)\Big)=\mathcal{O}(h^3).
\end{aligned}\tag{B.6}$$

At the same time-stage $t=\frac{\tau}{2}$, the reconstruction satisfies

$$\mathbb{T}u_{(i+\frac{1}{2},\pm),j+G}^{\frac{1}{2}}=\mathcal{O}(h^3),\quad \mathbb{T}\left(\partial_x u\right)_{(i+\frac{1}{2},\pm),j+G}^{\frac{1}{2}}=\mathcal{O}(h^3),\quad \mathbb{T}\left(\partial_y u\right)_{(i+\frac{1}{2},\pm),j+G}^{\frac{1}{2}}=\mathcal{O}(h^3).\tag{B.7}$$

Then with the same type of expansions we obtain at $t=\tau$

$$\mathbb{T}\bar{u}_{ij}^{1}=\mathcal{O}(h^5),\quad \mathbb{T}\bar{v}_{ij}^{1}=\mathcal{O}(h^4),\quad \mathbb{T}\bar{w}_{ij}^{1}=\mathcal{O}(h^4).\tag{B.8}$$

It follows that at terminal time $t^{tem}=\mathcal{O}(1)$ there holds

$$\mathbb{T}\bar{u}_{ij}^{tem}=\mathcal{O}(h^5)\cdot N=\mathcal{O}(h^4),\tag{B.9}$$

where N represents the times of time-stepping and $N=t^{tem}/\tau=\mathcal{O}(h^{-1})$, which implies the temporal accuracy is fourth order once the Hermite reconstruction attains desired order.

Under the original framework, numerical experiments show that using gradient averages as input for the reconstruction of gradients, reduces the temporal accuracy from fourth-order to third-order. Next, we try to explain the reasons for the order degeneracy under specific reconstructions. The line average along the interface $\hat{\boldsymbol{u}}_{i+\frac{1}{2},j+G}^{n+\frac{1}{2}}$ is calculated in the way

$$\hat{\boldsymbol{u}}_{i+\frac{1}{2},j+G}^{n+\frac{1}{2}}=\boldsymbol{u}_{i+\frac{1}{2},j+G}^{n,+}+\frac{\tau}{2}\left(\partial_t \boldsymbol{u}\right)_{i+\frac{1}{2},j+G}^{n,+}.\tag{B.10}$$

Then the second formula of (B.3) becomes

$$\mathbb{T}\hat{u}_{i+\frac{1}{2},j+G}^{\frac{1}{2}}=\mathbb{T}u_{(i+\frac{1}{2},-),j+G}^{0}+\frac{\tau}{2}\mathbb{T}\left(\partial_t u\right)_{i+\frac{1}{2},j+G}^{0,+}-\frac{\tau^2}{8}\partial_t^2 u(x_{i+\frac{1}{2}},y_{j+G},0)+\mathcal{O}(\tau^3).\tag{B.11}$$

Subsequently, the second and third formulae of (B.6) becomes

$$\begin{aligned}
&\mathbb{T}\bar{v}_{ij}^{\frac{1}{2}}=\frac{1}{h}\Big(\mathcal{O}(h^4)+\mathcal{O}(\tau h^3)+\mathcal{O}(\tau^2 h)+\mathcal{O}(\tau^3)\Big)=\mathcal{O}(h^2),\\
&\mathbb{T}\bar{w}_{ij}^{\frac{1}{2}}=\frac{1}{h}\Big(\mathcal{O}(h^4)+\mathcal{O}(\tau h^3)+\mathcal{O}(\tau^2 h)+\mathcal{O}(\tau^3)\Big)=\mathcal{O}(h^2),
\end{aligned}\tag{B.12}$$

and (B.7) becomes

$$\mathbb{T}u_{(i+\frac{1}{2},\pm),j+G}^{\frac{1}{2}}=\mathcal{O}(h^3),\quad \mathbb{T}\left(\partial_x u\right)_{(i+\frac{1}{2},\pm),j+G}^{\frac{1}{2}}=\mathcal{O}(h^2),\quad \mathbb{T}\left(\partial_y u\right)_{(i+\frac{1}{2},\pm),j+G}^{\frac{1}{2}}=\mathcal{O}(h^2).\tag{B.13}$$

Note that the accuracy of the approximate to $\partial_x u$ and $\partial_y u$ reduces to second-order, and we obtain

$$\mathbb{T}\bar{u}_{ij}^1 = \mathcal{O}(h^4), \quad \mathbb{T}\bar{v}_{ij}^1 = \mathcal{O}(h^3), \quad \mathbb{T}\bar{w}_{ij}^1 = \mathcal{O}(h^3). \tag{B.14}$$

Thus, the temporal order at the terminal time t^{tem} would reduces from fourth-order to third-order:

$$\mathbb{T}\bar{u}_{ij}^{tem} = \mathcal{O}(h^4) \cdot N = \mathcal{O}(h^3). \tag{B.15}$$

References

[1] A. Harten, B. Engquist, S. Osher, S. Chakravarthy, Uniformly high order essentially non-oscillatory schemes, III, Journal of Computational Physics 71 (1987) 231–303.

[2] C.-W. Shu, Essentially non-oscillatory and weighted essentially non-oscillatory schemes for hyperbolic conservation laws, in: Advanced Numerical Approximation of Nonlinear Hyperbolic Equations, Springer, 1998, pp. 325–432.

[3] C.-W. Shu, Essentially non-oscillatory and weighted essentially non-oscillatory schemes, Acta Numerica 29 (2020) 701–762.

[4] J. Qiu, C.-W. Shu, Hermite WENO schemes and their application as limiters for Runge-Kutta discontinuous Galerkin method: One-dimensional case, Journal of Computational Physics 193 (2004) 115–135.

[5] J. Qiu, C.-W. Shu, Hermite WENO schemes and their application as limiters for Runge-Kutta discontinuous Galerkin method. II: Two dimensional case, Computers & Fluids 34 (2005) 642–663.

[6] S. Gottlieb, D. Ketcheson, C.-W. Shu, Strong Stability Preserving Runge-Kutta and Multistep Time Discretizations, World Scientific, Singapore, 2011.

[7] P. Lax, B. Wendroff, Systems of conservation laws, Communications on Pure and Applied Mathematics 13 (1960) 217–237.

[8] J. Qiu, C.-W. Shu, Finite difference WENO schemes with Lax-Wendroff-type time discretizations, SIAM Journal of Scientific Computing 24 (2003) 2185–2198.

[9] D. C. Seal, Y. Güçlü, A. J. Christlieb, High-order multiderivative time integrators for hyperbolic conservation laws, Journal of Scientific Computing 60 (2014) 101–140.

[10] A. Christlieb, S. Gottlieb, Z. Grant, D. C. Seal, Explicit strong stability preserving multistage two-derivative time-stepping schemes, Journal of Scientific Computing 68 (2016) 914–942.

[11] J. Li, Z. Du, A two-stage fourth order time-accurate discretization for Lax–Wendroff type flow solvers I. Hyperbolic conservation laws, SIAM Journal of Scientific Computing 38 (2016) A3046–A3069.

[12] L. Pan, K. Xu, Q. Li, J. Li, An efficient and accurate two-stage fourth-order gas-kinetic scheme for the Euler and navier-stokes equations, Journal of Computational Physics 326 (2016) 197–221.

[13] Z. Du, J. Li, A Hermite WENO reconstruction for fourth order temporal accurate schemes based on the GRP solver for hyperbolic conservation laws, Journal of Computational Physics 355 (2018) 385–396.

[14] A. Li, J. Li, Lax-wendroff solvers-based Hermite reconstruction for hyperbolic problems, Applied Mathematics and Computation 447 (2023) 127915.

[15] M. Ben-Artzi, J. Li, G. Warnecke, A direct Eulerian GRP scheme for compressible fluid flows, Journal of Computational Physics 218 (2006) 19–43.

[16] G.-S. Jiang, C.-W. Shu, Efficient implementation of weighted ENO schemes, Journal of Computational Physics 126 (1996) 202–228.
[17] G. Capdeville, A central WENO scheme for solving hyperbolic conservation laws on non-uniform meshes, Journal of Computational Physics 227 (2008) 2977–3014.
[18] J. Zhu, C.-W. Shu, A new type of multi-resolution WENO schemes with increasingly higher order of accuracy, Journal of Computational Physics 375 (2018) 659–683.
[19] D. S. Balsara, S. Garain, C.-W. Shu, An efficient class of WENO schemes with adaptive order, Journal of Computational Physics 326 (2016) 780–804.
[20] M. Castro, B. Costa, W. S. Don, High order weighted essentially non-oscillatory WENO-Z schemes for hyperbolic conservation laws, Journal of Computational Physics 230 (2011) 1766–1792.
[21] N. A. Adams, K. Shariff, A high-resolution hybrid compact-ENO scheme for shock-turbulence interaction problems, Journal of Computational Physics 127 (1996) 27–51.
[22] X. Liu, S. Zhang, H. Zhang, C.-W. Shu, A new class of central compact schemes with spectral-like resolution II: Hybrid weighted nonlinear schemes, Journal of Computational Physics 284 (2015) 133–154.
[23] J. Li, C.-W. Shu, J. Qiu, Multi-resolution HWENO schemes for hyperbolic conservation laws, Journal of Computational Physics 446 (2021) 110653.
[24] E. Han, J. Li, H. Tang, Accuracy of the adaptive GRP scheme and the simulation of 2-D Riemann problems for compressible Euler equations, Communications in Computational Physics 10 (2011) 577–609.
[25] P. Woodward, P. Colella, The numerical simulation of two-dimensional fluid flow with strong shocks, Journal of Computational Physics 54 (1984) 115–173.